UNIVERSITY OF TURIN
COMPUTER SCIENCE DEPARTMENT

Master Thesis in Computer Science

Artificial Intelligence and Information Processing Systems

Integrating Anatomical Information in Weakly Contrastive Learning for Neuroimaging

Candidate: MATTEO BRUNELLO

Supervisor: MARCO GRANGETTO

Co-Supervisor: CARLO ALBERTO BARBANO

ACADEMIC YEAR 2023-2024

Abstract

In recent years, the application of deep neural networks, particularly Convolutional Neural Networks (CNNs), has yielded remarkable results across various domains that benefit from automated image analysis. The field of neuroimaging has particularly benefited from these advances, driven by the growing availability of brain imaging data, facilitated by enhancements in non-invasive acquisition methods like magnetic resonance imaging.

However, the application of deep learning in neuroimaging faces challenges, especially when applied to the prediction of psychiatric and neurological disorders, which encompasses a wide range of clinical, biological, and environmental factors. This challenge is further exacerbated by data scarcity. Although the volume of neuroimaging data has increased in recent years due to collaborative research efforts, these datasets are often limited in size, especially when focused on specific neurological conditions. To address these challenges, Transfer Learning and Contrastive Learning have emerged as effective strategies, showing good performances in various neuroimaging tasks compared to traditional machine learning approaches. According to this framework, a model is initially pre-trained on a large dataset of healthy subjects using Contrastive Learning techniques. Subsequently, this pre-trained model is fine-tuned for a specific task using a smaller cohort of patients, typically associated with a particular condition or phenotype.

Neuroimaging datasets are also rich in additional patient information, such as age, sex, and other neuroanatomical data. These features are valuable markers, particularly when correlated with data derived from neuroimaging studies. Recent research efforts have focused on integrating these features into the pre-training phase using contrastive learning techniques. However, current state-of-the-art methods predominantly rely on chronological age as the primary feature during pre-training, which may not sufficiently capture the complex information inherent in brain MRI data.

This thesis introduces a novel approach designed to overcome this limitation. The core of this research involves the development and application of a new Contrastive Learning method termed AnatCL, which integrates multiple anatomical measures derived from brain MRIs along with demographic data (patient age). By incorporating additional features, AnatCL facilitates the learning of more meaningful and generalizable representation spaces that more accurately reflect individual variability and aging patterns. Results from evaluating various downstream tasks across multiple neuroimaging datasets suggest that enriching these learning methods with additional data can yield more robust and generalizable models.

Acknowledgements

I would like to express my deepest gratitude to those who have supported me during this academic journey.

First and foremost, I extend my profound thanks to my supervisor, Marco, and co-supervisor, Carlo. Their invaluable support throughout the research process and the writing of this dissertation has been crucial. From the first day of working on this thesis, you have shown me great kindness and were exceptionally accessible for all matters, extending even beyond academics. If working on the thesis has been a very enjoyable experience for me, it is largely thanks to you.

I must also extend a heartfelt thank you to my parents. Their steadfast support and belief in my abilities have afforded me the opportunity to pursue my studies. Their love and patience, especially during the most challenging times, have been my foundation. Without their sacrifices and encouragement, none of this would have been possible.

My journey at the university was also enriched by peers who became close friends. To Edoardo and Giuseppe, with whom I've shared the long and memorable journey of university life, thank you. The unforgettable moments we shared truly brightened my days.

Finally, I would like to thank my girlfriend, Cecilia. Even though you joined me during the final stretch of this beautiful journey, you have proven to be an invaluable partner, both patient and always ready to listen. I also extend my gratitude to all other friends who have been part of this journey, whose companionship and support have been invaluable. Thank you all for being part of this story.

Contents

List of Figures

List of Tables

Introduction 1

1.1 Background and Motivation

Neuroimaging has come up as a pivotal tool in understanding the structure and function of the human brain. Amongst the neuroimaging techniques available, MRI is the most popular, being a non-invasive technique that has high spatial resolution. MRI has broad application in diagnosis and studies related to neurological disorders, including but not limited to Alzheimer's Disease, schizophrenia, and Autism Spectrum Disorder (ASD). Further advancements in hardware and software techniques have also enabled the development of various MRI modalities, each serving unique purposes in brain imaging, with the most notable ones being:

- Structural Magnetic Resonance Imaging (sMRI), which provides high-resolution images that assess the morphology, volume, and other anatomical measures[1] of the brain.
- Functional Magnetic Resonance Imaging (fMRI), which measures brain activity by detecting changes associated with blood flow.
- Diffusion Magnetic Resonance Imaging (dMRI), which maps the diffusion process of molecules in biological tissues, highlighting neural pathways in the brain.

1: For instance, one such measure is the *cortical thickness*, which refers to the thickness of the cerebral cortex, the outer layer of the brain that is responsible for high-level cognition and functions.

The advancement of MRI technology has brought numerous benefits, opening up many possibilities for automated analysis methods. This is particularly important as neurological disorders encompasses multiple factors that must be considered simultaneously, requiring a multifaceted evaluation. In this context, the application of computer vision methods may be beneficial, especially for the extraction and analysis of complex patterns within the images that may be too subtle or intricate for manual detection.

In recent years, the advancements in computer vision propelled by Deep Learning [1], have introduced exceptional tools for image recognition, segmentation, and classification. In particular, Convolutional Neural Networks [2] have shown very strong performance in the capture of hierarchical features in visual data. These advances have brought a new

[1]: LeCun et al. (2015), *Deep learning*

[2]: LeCun et al. (1989), *Handwritten Digit Recognition with a Back-Propagation Network*

source of inspiration for neuroimaging analysis. However, the employment of such models in neuroimaging also introduces some unique challenges such as:

- High dimensionality and complexity of data: brain MRI scans produce complex and high-dimensional data that encapsulates intricate anatomical information that requires more data for models to learn the statistical correlations. The inherently three-dimensional nature of MRI data presents significant challenges compared to conventional two-dimensional image representation models. This issue is particularly pronounced in scenarios where data is scarce, compounding the difficulty of training effective models.
- Limited annotated data: high cost of manual annotation, coupled with necessary expert knowledge imposition, makes the scale of labeled neuroimaging data hard to achieve. This practice, therefore, makes it difficult to achieve generalization capability of supervised deep learning models, often induced by label noise or performance degradation upon transfer to unseen data.
- Anatomical variability between subjects: the anatomical variation of the human brain is large between subjects. Furthermore, it is largely influenced by factors such as age, sex, and neurological diseases. This makes the development of deep learning models that can work well across these diverse populations a real challenge.

All these issues can largely be attributed to a lack of annotated data, a problem that is particularly accentuated in the field of neuroimaging. Despite recent efforts to increase the collection of neuroimaging data, these datasets remain relatively small compared to those available in other imaging fields. This limitation is even more pronounced for datasets concerning specific neurological conditions that are demographically rare, exacerbating the challenges of developing robust and effective models due to the limited availability of comprehensive data.

The principle of Transfer Learning helps mitigate the challenges associated with the scarcity of labeled data. This method begins by training the target model in a self-supervised manner using a large unlabeled dataset[2]. The underlying rationale of this first phase is to enable the model to learn the basic statistical correlations present in the general population. Subsequently, the model is fine-tuned for a specific

2: In neuroimaging, unlabeled data consist of MRI scans.

downstream task[3], typically using a smaller labeled dataset. This two-stage approach leverages the broad generalizability learned initially and applies it to more focused, specific tasks, enhancing the model's performance on datasets where labeled examples are limited.

3: Example tasks may be brain age or patient's sex prediction.

One of the pre-training methods that has shown considerable success in the literature is Contrastive Learning [3–8]. The unsupervised form of this method is a learning paradigm that aims to minimize the distance between positive pairs[4] and maximize the distance between negative pairs in a latent space that the model must learn. Despite its effectiveness compared to other self-supervised learning methods, Contrastive Learning has inherent limitations, notably that positive samples with respect to the anchor may inadvertently be treated as negative samples. Such misclassification can potentially hinder the model's ability to learn accurate representations, especially in complex datasets where similar but distinct classes may exist.

4: Different augmentations of the same image (referred to as the *anchor*) constitute positive pairs, whereas augmentations from different images form negative pairs.

To address this issue, it is possible to utilize additional metadata associated with each sample[5] to more accurately determine whether a sample should be considered positive or negative relative to the anchor. Incorporating such metadata can enhance the model's ability to discern between positive and negative pairs, resulting in more informative and generalizable representation spaces that translates in better performance in downstream tasks. These approaches are categorized as *weakly supervised learning* methods because they leverage an indirect source of information about the target task rather than relying on direct and precise labels.

5: This metadata typically remains unused in self-supervised methods.

Existing weakly supervised contrastive learning approaches focus on the integration of continuous attributes like brain age, achieving state-of-the-art performance in brain age prediction. However, these methods are limited to a single attribute, leaving most other meta-information that is present in neuroimaging datasets unused. This work builds upon existing state-of-the-art methods by incorporating additional meta-information along with age. The proposed framework is AnatCL, a novel contrastive loss that leverages both age and anatomical brain measures. Models pre-trained with AnatCL outperform current SOTA approaches on various downstream tasks, suggesting that it could become an effective framework for pre-training foundation models in brain imaging.

1.2 Contributions of this Work

The research work discussed in this thesis has been summarized in a research paper [9] that was submitted to the NeurIPS conference.

[9]: Barbano et al. (2024), *Anatomical Foundation Models for Brain MRIs*

1.3 Thesis Structure

This thesis is divided into two parts. The first part includes all the chapters presenting the background information needed to understand the following parts. These chapters take a focused approach, introducing only the elements that are needed further on, without discussing extensively the entire literature, which is outside the scope of this thesis. Building from first principles, Chapter 2 introduces the basic methods, algorithms and models typical of deep learning, with a focus on imaging models. Chapter 3, on the other hand, gives a bird's eye view of various acquisition methods, preprocessing and analysis of neuroimaging data.

The second part presents the main body of the thesis, discussing the novel loss formulation, experiments, and potential future developments. Specifically, this section is organized into several chapters: Chapter 4 discusses the loss formulation, Chapter 5 provides a comprehensive account of the experiments conducted to evaluate the proposed loss, and Chapter 6 explores potential future research directions stemming from this work. Each chapter is designed to stand alone, allowing readers with sufficient background knowledge to directly engage with specific sections of interest. For instance, machine learning practitioners who are familiar with the foundational concepts may prefer to start with Chapter 3 before proceeding to Chapter 4 to gain a deeper understanding of the context and application of the novel methodologies discussed. On the other hand, neuroimaging practitioners may prefer to first explore the chapter dedicated to deep learning (Chapter 2) before delving into the methodologies discussed in Chapter 4.

Deep Learning 2

Differentiable programming [10, 11] represents a paradigm where the algorithms and functions within a program are designed to be differentiable. This capability allows for the automatic adjustment of parameters based on the data they process, facilitating the application of gradient-based optimization methods. Essentially, differentiable programming turns traditional programming constructs into learnable and adaptable entities, enabling the development of systems that can efficiently learn from vast datasets and complex environments.

[10]: Blondel et al. (2024), *The Elements of Differentiable Programming*
[11]: Scardapane (2024), *Alice's Adventures in a Differentiable Wonderland – Volume I, A Tour of the Land*

The roots of differentiable programming can be traced back to the early applications of calculus in computational tasks, where differentiation and integration were used to solve physics-based and engineering problems. With the advent of digital computing, these methods were translated into algorithms that could be executed on machines. Over time, as the need for more sophisticated data analysis and modeling grew, especially with the burgeoning field of artificial intelligence, the methods evolved into what we now recognize as differentiable programming.

The concept gained significant traction in the late 20th and early 21st centuries, driven by the growth of machine learning and particularly the resurgence of neural networks. The development of automatic differentiation technologies marked a pivotal advancement, making it practical to implement and train complex models that require the efficient calculation of derivatives. By blurring the lines between traditional programming and machine learning, differentiable programming has created a new toolbox for problem solving, one that is inherently flexible, powerful, and suited to a range of applications that extend far beyond its origins. This blend of flexibility and power forms the bedrock upon which modern machine learning, especially deep learning, builds to achieve remarkable feats across various domains.

Deep learning [1, 12] stands as a prominent example of differentiable programming in action, illustrating the power and versatility of this computational paradigm. At its core, deep learning involves systems that are intricately designed to learn from data by approximating functions that map

[1]: LeCun et al. (2015), *Deep learning*
[12]: Goodfellow et al. (2016), *Deep Learning*

inputs to desired outputs. These mappings are not fixed; instead, they are dynamically refined through the model's learnable parameters, which fundamentally determine the output of the function. For example, Equation 2.1 illustrates a series of parameterized maps, each with one and two parameters respectively (θ_0 and θ_0, θ_1 respectively).

$$f(x;\theta) = \theta_0 x \quad f(x;\theta) = \theta_0 x + \theta_1 x \tag{2.1}$$

The optimization of these parameters is where the principles of differentiable programming become essential. Deep learning models adjust their parameters [1] based on the input data they receive and the feedback (loss[2]) related to the accuracy of their outputs. This adjustment is achieved through gradient-based optimization methods, a process central to the training and effectiveness of deep learning systems. From this discussion it's possible to clearly delineate the main components essential to deep learning:

1: Namely weights and biases.

2: Which measure how far the model's predictions deviate from the actual values.

- **Model**: a function $f(x;\theta)$ parametrized by θ.
- **Dataset**: a supervised dataset $\mathscr{D}_n$ of size n is a set of n pairs $\mathscr{D}_n = \{(x_i, y_i)\}_{i=1}^{n}$, where each (x_i, y_i) is an example of an input-output relationship that the model must approximate.
- **Loss**: a *differentiable* function $L(y, \hat{y})$ that given a desired target y and the predicted value $\hat{y} = f(x)$, qualifies the discrepancy between the model's prediction and the actual value y.
- **Optimization method**: an algorithm that adjusts the model's parameters θ to minimize the average loss across the entire dataset.

As previously discussed, the essence of deep learning involves developing models that approximate the relationship between inputs and outputs using only a limited subset of data points (the dataset). These models learn from this dataset by minimizing a loss function, which quantifies the extent of incorrect predictions. Building on the definitions provided earlier, this learning process can be structured as an optimization problem.

$$\theta^* = \arg\min_{\theta} \frac{1}{n} \sum_{i=1}^{n} L(y_i, f(x_i;\theta)) \tag{2.2}$$

Equation 2.2 formalizes the objective of the optimization problem in deep learning, which involves identifying a set of parameters θ that minimizes the average loss across the entire dataset. This method approximates the expected loss across the general distribution, ensuring that the model $f(x;\theta^*)$ is optimally accurate in mapping inputs to their correct outputs by closely estimating the true risk[3] with the available data.

3: The optimization problem adheres to the empirical risk minimization (ERM) principle, which leverages the law of large numbers to approximate how well a predictive model will perform in practice. Since the true distribution of data is unknown, ERM focuses on minimizing the observed loss on a specific dataset, referred to as the "empirical risk."

2.1 Gradient Based Optimization

To solve the optimization problem formalized in Equation 2.2, gradient-based optimization methods are predominantly employed, especially in deep learning. These methods are highly effective due to their ability to manage the complexities and extensive scale of neural network training, and are particularly well-suited for navigating the intricate loss landscapes that arise from the non-linear activation functions typical of deep networks. Unlike simpler models, deep learning architectures often feature complex, non-convex loss functions that lack analytical solutions, making gradient-based approaches essential for finding approximate solutions. A significant advantage of gradient-based methods is their flexibility and generality, which allows them to be applied across a wide range of problem settings and architectures without specific tailoring to the task. This versatility is enhanced by their efficiency in high-dimensional spaces, a common feature in neural networks that often include millions of parameters. Gradient-based optimization methods rely on calculating the *gradient*[4] $\nabla_\theta L$ of the loss function L with respect to the model's parameters θ. The optimization method then iteratively adjusts the parameters in the opposite direction of the gradient.

4: A gradient is the generalization of the concept of a derivative to functions of multiple variables. While a derivative gives the rate of change of a function with respect to one variable, the gradient extends this idea to vector fields. The gradient is then a vector that points to the direction of the steepest ascent of a function in any specific point.

$$\theta_t = \theta_{t-1} - \gamma \cdot \nabla_\theta \left(\frac{1}{n} \sum_{i=1}^{n} L(y_i, f(x_i; \theta_{t-1})) \right) \tag{2.3}$$

Equation 2.3 shows the update rule applied at each iteration, where the parameters for the next iteration, θ_t, are derived by reducing the current parameters θ_{t-1} by a small fraction of the gradient of the expected loss across the dataset. This fraction is governed by γ, commonly referred to as the *learning rate*, which directly influences the magnitude of each step in the iterative process. The update rule is typically applied over a number of iterations referred to as *epochs*, which correspond to the number of times the entire dataset is processed.

Geometrically, this update rule can be visualized as a method for navigating the multidimensional landscape defined by the loss function. Here, θ represents a point in this landscape, and the gradient of the loss function at this point indicates the direction of steepest ascent. By moving in the opposite direction, which is the negative gradient, the update rule effectively seeks the path of steepest descent, thereby taking steps that effectively minimize the loss.

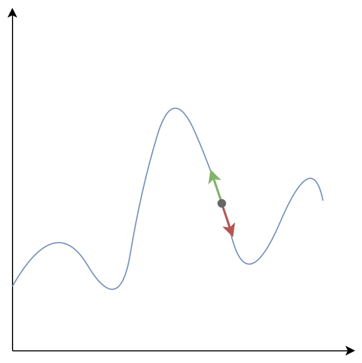

Figure 2.1: The gradient (green arrow) of a function evaluated in a specific point (gray) indicates the direction of the steepest ascent from that point. Conversely, the opposite of the gradient (red arrow) indicates the direction of the steepest descent.

This method of using gradients to optimize function parameters, highlights a crucial aspect of differentiable programming: every component of the computational model, especially those that impact learning and prediction, needs to be differentiable in terms of their parameters. Moreover, the effectiveness of the optimization hinges directly on the efficiency with which gradients are computed. Consequently, it is essential to have a robust method for this computation to ensure the optimization process is both accurate and efficient.

2.1.1 Automatic Differentiation

Automatic differentiation (AD) is a computational technique that efficiently and accurately computes derivatives of functions. Unlike symbolic differentiation, which manipulates mathematical symbols to produce derivative formulas, or numerical differentiation, which approximates derivatives using finite differences, AD operates directly on numerical values and applies the chain rule to compute derivatives of composed functions. To fully understand the utility and mechanics of Automatic Differentiation and the specific challenges it addresses, it is crucial to first explore the two prevalent methods used to compute derivatives on a computer. The first is *symbolic differentiation*, which involves manipulating the mathematical symbols of the original expression through a set of transformation rules[5]. By systematically applying these rules, one can derive an expression that can be used to compute the gradient at any point, provided that the derivative is continuous. Symbolic differentiation is considered stable in that it does not introduce computational error. However, it is often challenging to implement and can be computationally inefficient compared to other methods, particularly as the function expressions become more complex and the expressions for their derivatives increase drastically

5: For instance, the derivative $\frac{\partial \sin(x)}{\partial x}$ is $\cos(x)$.

in the number of terms. This exponential growth in complexity can significantly hinder performance and scalability. The second approach to computing derivatives, known as *numerical differentiation* or the *finite difference* method, utilizes the conventional definition to calculate the derivative at a specific point. Equation 2.4 shows the standard formula for divided differences, which calculates the slope of the secant line through the points $(x, f(x))$ and $(x + h, f(x + h))$. By selecting an infinitesimally small value for h, it is possible to achieve an increasingly accurate approximation of the true derivative.

$$f'(x) = \lim_{h \to 0} \frac{f(x + h) - f(x)}{h} \tag{2.4}$$

While generally being more computationally efficient than the former (as it does not require the precomputation of the derivative expression), a significant drawback of this approach is its numerical stability; it can introduce round-off errors during the discretization process, particularly when computing derivatives of orders higher than the first. This susceptibility to errors stems from the finite precision with which computers represent numbers, which can lead to inaccuracies in the calculated derivatives, especially for small differences in function values.

Generally speaking, numerical differentiation is particularly useful when the exact analytical derivative is difficult to obtain, as it allows for the practical estimation of derivatives using straightforward numerical computations.

Both classical methods of differentiation, symbolic and numerical, have their advantages and disadvantages. However, their primary drawback lies in the slow computation of partial derivatives of a function with respect to multiple inputs, which is essential for gradient-based optimization algorithms[6]. Automatic differentiation effectively resolves all these issues by providing a more efficient and rapid means to calculate these derivatives, thereby enhancing the performance of algorithms that rely heavily on gradient calculations.

6: Especially in deep learning, where the gradient with respect to million of parameters must be computed at each iteration of the learning process.

Automatic differentiation capitalizes on the principle that all functions, regardless of their complexity, are ultimately reducible to a sequence of elementary arithmetic operations (such as addition, subtraction, multiplication, and division) and elementary functions (like exp, log, sin, and cos). The key idea of AD involves breaking down computations into elementary steps that create an *evaluation trace* [13]. Each step's derivative is then integrated using the chain rule. Thanks to the utilization of evaluation traces, AD is capable of differentiating not only through calculations in closed form

[13]: Griewank et al. (2008), *Evaluating Derivatives*

but also through control flow statements commonly found in programming. Regardless of the specific computational pathway executed, the numerical operations will generate an evaluation trace that can be employed for AD. An evaluation trace can be seen as the series of steps that are needed to reach the final result. Consider, for example, the function $f : \mathbb{R}^n \longrightarrow \mathbb{R}^m$ (where $n = 2$ and $m = 1$) whose expression is provided in Equation 2.5.

Table 2.1: Evaluation trace of Equation 2.5.

Variable	Expression	Value
v_{-1}	x_1	1.5
v_0	x_2	0.5
v_1	v_{-1}/v_0	3.0
v_2	$sin(v_1)$	0.141
v_3	$exp(v_0)$	1.648
v_4	$v_1 - v_2$	1.351
v_5	$v_2 + v_4$	1.492
v_6	$v_5 \cdot v_4$	2.016

$$y = \left[\sin\left(\frac{x_1}{x_2}\right) + \frac{x_1}{x_2} - \exp\left(x_2\right)\right]\left[\frac{x_1}{x_2} - \exp\left(x_2\right)\right] \tag{2.5}$$

Using the following notation:

- $v_{i-n} = x_i, i = 1, \dots, n$ are the input variables.
- $v_i, i = 1, \dots, l$ are the intermediate variables.
- $y_{m-i} = v_{l-i}, i = (m-1), \dots, 0$ are the output variables.

The expression shown in Equation 2.5 can be decomposed into simpler components as shown in Equation 2.6. By assigning values to each input, x_1, x_2, and sequentially evaluating each sub-expression, the final value of y can be obtained[7].

7: This procedure corresponds to executing the differentiable program f, a process often referred to in deep learning as the *forward pass*. This term underscores the transformation of the input signal through intermediate steps until the output is reached

$$\begin{aligned} v_{-1} &= x_1 \\ v_0 &= x_2 \\ v_1 &= v_{-1}/v_0 \\ v_2 &= sin(v_1) \\ v_3 &= exp(v_0) \\ v_4 &= v_1 - v_3 \\ v_5 &= v_2 + v_4 \\ v_6 &= v_5 \cdot v_4 \end{aligned} \tag{2.6}$$

For example, a possible run with $x_1 = 1.5$ and $x_2 = 0.5$ would lead to the evaluation trace depicted in Table 2.1. This evaluation trace is also called *Wengert List* [14]. A logical progression in determining the derivative of y with respect to its inputs involves following the evaluation trace and computing the derivatives sequentially for each intermediate variable. This approach forms the basis of the *forward mode* of the automatic differentiation algorithm.

[14]: Wengert (1964), *A simple automatic derivative evaluation program*

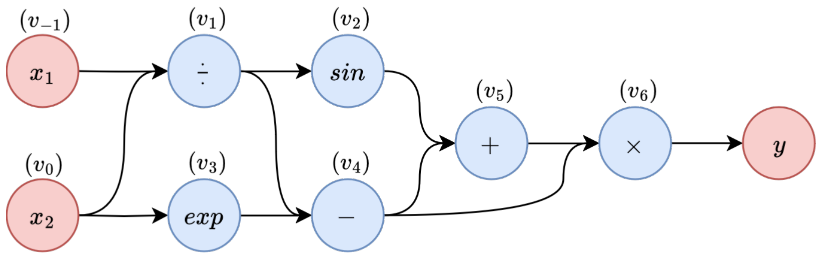

Figure 2.2: Equation 2.6 can also be represented graphically as a Directed Acyclic Graph (DAG). In this representation, blue nodes symbolize the intermediate operations, red nodes denote the input/output nodes, and the edges depict the algebraic relationships between these nodes.

Forward Mode

Suppose the objective is to compute the derivative $\frac{\partial y}{\partial t}$ with respect to an arbitrary input variable t. The chain rule (Equation 2.7), offers a straightforward method for accomplishing this.

$$\frac{\partial u}{\partial t} = \sum_i \left(\frac{\partial u}{\partial v_i} \frac{\partial v_i}{\partial t} \right) \tag{2.7}$$

The forward method of automatic differentiation involves calculating the derivative $\dot{v}_i = \frac{\partial v_i}{\partial t}$ for each intermediate variable v_i. According to the chain rule (Eq. 2.7), the derivative of each variable v_i is dependent on the values preceding it, allowing gradients to be accumulated throughout the forward pass. This process is therefore aptly named the *forward accumulation mode*. To illustrate the dependency chain integral to the process of forward accumulation, Equation 2.8 demonstrates the computation of the derivative $\dot{v}_1$, emphasizing that the current derivative value ($\dot{v}_1$) is contingent upon both the values and derivatives of preceding variables (v_0, v_{-1}).

Equation 2.7 illustrates the application of the chain rule in computing the gradient of u with respect to any intermediate variable t. The computation involves summing the products of each partial derivative of u with respect to its intermediate variables v_i and the gradient of each intermediate variable v_i with respect to the input t.

$$\begin{aligned} \dot{v}_1 &= \frac{\partial v_1}{\partial t} \\ &= \frac{\partial v_1}{\partial v_{-1}} \frac{\partial v_{-1}}{\partial v_t} + \frac{\partial v_1}{\partial v_0} \frac{\partial v_0}{\partial v_t} \\ &= \frac{\partial v_1}{\partial v_{-1}} \dot{v}_{-1} + \frac{\partial v_1}{\partial v_0} \dot{v}_0 \\ &= \frac{1}{v_0} \dot{v}_{-1} + \dot{v}_0 \left(-\frac{v_{-1}}{v_0^2} \right) \end{aligned} \tag{2.8}$$

By applying the same rule to each variable v_i, it is possible to derive the formulas to compute the gradient of each intermediate variable of the computation, as demonstrated in Equation 2.9.

$$\begin{aligned}
\dot{v}_{-1} &= \frac{\partial x_1}{\partial t} \\
\dot{v}_0 &= \frac{\partial x_2}{\partial t} \\
\dot{v}_1 &= \frac{1}{v_0}\dot{v}_{-1} + \dot{v}_0 \left(-\frac{v_{-1}}{v_0^2}\right) \\
\dot{v}_2 &= cos(v_1)\dot{v}_1 \\
\dot{v}_3 &= exp(v_0)\dot{v}_0 \\
\dot{v}_4 &= \dot{v}_1 - \dot{v}_3 \\
\dot{v}_5 &= \dot{v}_2 + \dot{v}_4 \\
\dot{v}_6 &= v_4\dot{v}_5 + v_5\dot{v}_4
\end{aligned} \tag{2.9}$$

Equation 2.9 thus presents a generic method for computing the derivative of v_i with respect to any input variable t. To leverage this method, one must set the derivative of the selected input variable relative to itself to 1, while all other input variable derivatives are set to 0. Subsequently, both v_i and $\dot{v}_i$ are sequentially computed at each i^{th} step. This approach yields two outcomes for each computation: the value of the expression and its derivative. The comprehensive record of derivative values is known as the *tangent trace*.

In forward mode, each node in the computational graph computes both the value of the node v_i and its derivative $\dot{v}_i$.

To illustrate this method, consider evaluating the derivative $\frac{\partial y}{\partial x_1}$ $(t = x_1)$ at the point $x_1 = 1.5$ and $x_2 = 0.5$ using the forward accumulation method. As discussed earlier, it is necessary to initialize $\dot{v}_{-1} = 1$ (and accordingly $\dot{v}_0 = 0$) and proceed with a sequential evaluation of the program[8]. The corresponding evaluation trace, along with its tangent trace, is detailed in Table 2.2.

8: Note that to obtain $\frac{\partial y}{\partial x_2}$, one must repeat the process, but setting $\dot{v}_0 = 1$ and $\dot{v}_{-1} = 0$.

Table 2.2: Evaluation trace of Equation 2.5 along with its tangent trace computed from Equation 2.9.

Variable	Value	Derivative
v_{-1}	1.5	1
v_0	0.5	0
v_1	3.0	2
v_2	0.141	−1.98
v_3	1.648	0
v_4	1.351	0
v_5	1.492	2
v_6	2.016	3.01

The forward accumulation method has been described using a function $f : \mathbb{R}^2 \longrightarrow \mathbb{R}^1$ but can be extended to any vector-valued real function $f : \mathbb{R}^n \longrightarrow \mathbb{R}^m$. This method is particularly advantageous when $m \gg n$, because its computational complexity is $O(n)$, correlating directly with the number of input dimensions of the function that requires differentiation. This efficiency stems from the necessity to repeat the forward and tangent computations for each input variable. Thus the forward method is not suitable in the context of optimizations of neural networks, where derivatives must be computed with respect to millions of parameters. Specifically, in the context of deep neural networks optimization, the class of vector valued functions are the loss functions, which have with a single output $m = 1$ and must be derived with respect to millions of parameters $n \approx 10^6$.

Reverse Mode

Reverse mode automatic differentiation builds upon the concept that derivatives can be computed from the end of the evaluation trace backwards to the beginning, which is the reverse of the forward mode approach. This method is based on the application of the chain rule (Equation 2.7), which, rather than being applied from inputs to outputs, is utilized from outputs back to inputs. Equation 2.10 illustrates this principle, where v_j represents all variables for which v_i serves as an input, and u denotes any output variable.

$$\frac{\partial u}{\partial v_i} = \sum_j \left(\frac{\partial u}{\partial v_j} \frac{\partial v_j}{\partial v_i} \right) \tag{2.10}$$

From a practical standpoint, reverse mode automatic differentiation (AD) does not substantially differ from forward mode AD. It involves computing the derivative $\bar{v}_i = \frac{\partial y}{\partial v_i}$ for each intermediate variable, referred to as the *adjoint* of v_i. Utilizing Equation 2.10 simplifies this process [9].

9: It is important to note that since the chain rule is applied from the output back to the inputs, it must be executed in *reverse order*. This means that, unlike in forward mode where computation might start with v_0 and v_{-1}, in reverse mode it begins from the final variable, such as v_6.

$$\begin{aligned}
\bar{v}_6 &= \frac{\partial y}{\partial v_6} (= 1) \\
\bar{v}_5 &= \bar{v}_6 v_4 \\
\bar{v}_4 &= \bar{v}_6 v_5 + \bar{v}_5 \\
\bar{v}_3 &= -\bar{v}_4 \\
\bar{v}_2 &= \bar{v}_5 \\
\bar{v}_1 &= \bar{v}_4 + \bar{v}_2 cos(v_1) \\
\bar{v}_0 &= \bar{v}_1 - \frac{v_{-1}}{v_0^2} + \bar{v}_3 \exp(v_0) \\
\bar{v}_{-1} &= \frac{\bar{v}_2}{v_0}
\end{aligned} \tag{2.11}$$

Equation 2.11 clearly demonstrates that in the computation of adjoints, each step is dependent either on the values of subsequent steps or the adjoints of these subsequent steps. Consequently, it is necessary to complete the computations for $\bar{v}_i$ *after* determining the values of v_i and the adjoints of subsequents steps $\bar{v}_k$ where $k > i$. Therefore, to compute

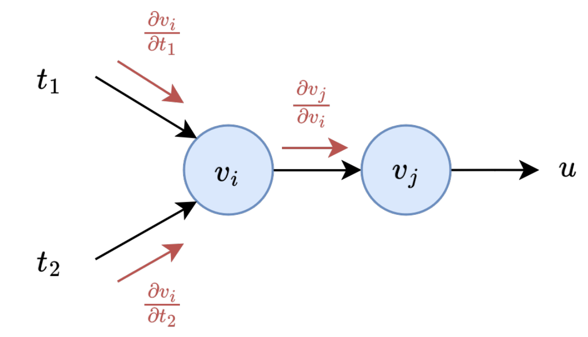

$\frac{\partial v_i}{\partial t_1}$
t_1
$\frac{\partial v_j}{\partial v_i}$
v_i
v_j
u
t_2
$\frac{\partial v_i}{\partial t_2}$

(a) Forward mode

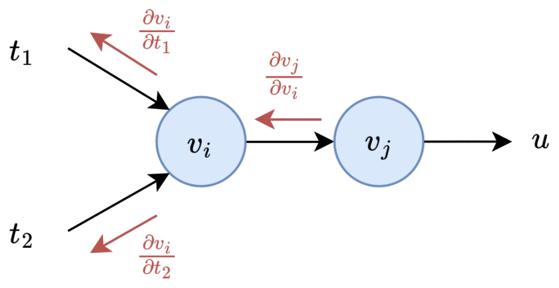

$\frac{\partial v_i}{\partial t_1}$
t_1
$\frac{\partial v_j}{\partial v_i}$
v_i
v_j
u
t_2
$\frac{\partial v_i}{\partial t_2}$

(b) Backward mode

Figure 2.3: Graphically, interpreting the chain rule in forward mode involves propagating gradients from inputs to outputs. Subfigure 2.3a visually illustrates this process, showing how node v_i transmits its derivative to the subsequent node v_j. Conversely, the backward mode entails the propagation of gradients from outputs back to inputs, as depicted in subfigure 2.3b. This graphical interpretation also clarifies how the automatic differentiation (AD) algorithm functions: to compute the derivative of a variable u with respect to another variable t, it simply involves multiplying the gradients that appear along the path from u to t.

derivatives using this method, the entire expression must first be executed to ascertain each v_i value. Subsequently, the derivative of the output variable with respect to itself must be initialized to 1, as exemplified here with $\frac{\partial y}{\partial v_6} = 1$. Following this initialization, the gradient computations can proceed in reverse, beginning from the output variables and progressing towards the input variables, following the same order as Equation 2.11.

Upon completing the backward mode of automatic differentiation, the adjoints of the input variables are determined. These adjoints represent the partial derivatives of y with respect to the input variables. This aspect underscores the efficiency of the reverse method: a single application of reverse mode yields the gradients for all input variables. With only two traversals of the computation graph (one forward and one backward) the method achieves a computational complexity of $O(2n)$. This efficiency makes it particularly suitable for computing the gradients of loss functions with respect to the parameters in deep neural networks[10], a crucial step in gradient-based optimization. Today, reverse mode automatic differentiation is the de facto standard for computing derivatives in the field. Common deep learning frameworks (or AD engines) such as PyTorch [15] and TensorFlow [16] internally represent computations as graphs and apply reverse mode automatic differentiation to compute the derivatives on these graphs.

10: In the context of deep learning, reverse mode automatic differentiation is commonly referred to as *backpropagation*.

[15]: Paszke et al. (2017), *Automatic differentiation in PyTorch*

[16]: Abadi et al. (2016), *Tensorflow: A System for Large-Scale Machine Learning*

Reverse mode automatic differentiation (AD) is highly efficient for computing gradients, but it does have a drawback concerning memory efficiency. Since the values of each intermediate step need to be available before initiating the backward pass, the entire evaluation trace must be stored in memory. This requirement can become unfeasible, particularly when dealing with large datasets or deep neural network models that involve extensive computational graphs. Such memory demands can limit the scalability of reverse mode AD in resource-constrained environments or when training extremely large models.

2.1.2 Stochastic Gradient Descent

As previously mentioned, gradient-based optimization methods compute the gradient of the expected loss with respect to the model's parameters. By examining the update rule in Equation 2.3, it is evident that the gradient computation of the expected loss can become problematic. This is due to the fact that, as the dataset size increases, memory and computational requirements for reverse mode automatic differentiation to compute the gradient would escalate significantly, rendering the method impractical for extremely large datasets. In practical applications, a variant of gradient descent known as Stochastic Gradient Descent (SGD) is commonly used. The fundamental concept of SGD involves sampling a subset $\mathcal{B}_r \subset \mathcal{D}_n$ (where $r \ll n$) at each iteration t. Utilizing this subset allows for the computation of an approximated version of the true expected loss, as demonstrated in Equation 2.12.

$$\frac{1}{r} \sum_{(x_i, y_i) \in \mathcal{B}_r} L(y_i, f(x_i; \theta)) \approx \frac{1}{n} \sum_{(x_i, y_i) \in \mathcal{D}_n} L(y_i, f(x_i; \theta)) \quad (2.12)$$

If the samples of the minibatch are independent and identically distributed from the dataset, the left-hand side of Equation 2.12 constitutes a Monte Carlo approximation of the full loss, and the same principle also applies to its gradient. The computational complexity of this process grows only with r, which users can directly control[11].

11: In practical terms, selecting smaller minibatch sizes (r) leads to more computationally efficient iterations but introduces higher variance in the gradient estimates. Conversely, larger r values produce more accurate gradient estimations but result in less efficient iterations. This trade-off between efficiency and accuracy must be carefully managed to optimize the learning process.

2.2 Neural Networks

Now that the foundational knowledge on how to train deep learning models has been established, the focus shifts to the models themselves. Previously, the model was defined as a plain function to abstract away the real components and inner workings, which will be discussed extensively in this section. Neural networks vary from simple to highly complex architectures, each possessing distinct capabilities and applications. However, all of these architectures are constructed with high-level differentiable components, such as neurons and layers[12].

12: To draw a parallel with conventional programming, these components can be seen as the basic constructs of differentiable programming.

2.2.1 Perceptron

[17]: Rosenblatt (1958), *The Perceptron: A Probabilistic Model for Information Storage and Organization in the Brain*

The Perceptron [17] represents one of the earliest models in the field of artificial neural networks, and serves as the basic building block the complex models that can be found today. The perceptron draws inspiration by the biological neuron, which, in a simplified view, functions by receiving a series of electrical input signals (coming from other neurons) that are collectively processed[13]. These synaptic weights can change through a process called synaptic plasticity, which is crucial for learning and memory. The perceptron mimics this mechanism with these main components:

13: Synaptic strengths, or synaptic weights, determine the influence of one neuron's signal on another.

- **Input nodes**: a vector $\mathbf{x}$ whose the single entry x_i represents the signal strength coming from the i^{th} input.
- **Weights**: a vector $\mathbf{w}$ that determines the synaptic strength of each input.
- **Bias**: a real value b that can be likened to the neuron's resting membrane potential[14].
- **Activation function**: a real valued function $\sigma : \mathbb{R} \to \mathbb{R}$ that determines whether the perceptron will activate or not based on its activation field[15].

14: The resting membrane potential is the baseline level of electrical charge inside the neuron relative to the outside.

15: The activation field of a perceptron is the weighted sum of the inputs plus the bias

Equation 2.13 shows the output of the perceptron model, utilizing all the previously discussed components. Note that the function is parameterized by the vector of weights and the bias. Consequently, the optimization process will adjust these parameters to enable the model to learn effectively.

$$\begin{aligned} f(\mathbf{x};\mathbf{w},b) &= \sigma\left(b + \sum_i \mathbf{w}_i \cdot \mathbf{x}_i\right) \\ &= \sigma(b + \mathbf{w}\cdot\mathbf{x}) \end{aligned} \tag{2.13}$$

Frequently, another formulation for the perceptron model is preferred, where the bias term b is *"absorbed"* into the weight vector $\mathbf{w}$ by setting the first weight variable $\mathbf{w}_0 = b$ and fixing the first input entry to always be $x_0 = 1$. The resulting formulation in Equation 2.14 is equivalent to that in Equation 2.13, offering a more compact notation that simplifies readability.

$$f(\mathbf{x};\mathbf{w}) = \sigma\left(\sum_i \mathbf{w}_i \cdot \mathbf{x}_i\right) \tag{2.14}$$

The perceptron model is particularly adept at solving linear classification problems by identifying a hyperplane that separates data points into two distinct classes within a multi-dimensional space. It excels in scenarios where the classes can be divided by a straight line in two dimensions, a plane in three dimensions, or a hyperplane in higher dimensions. If such a hyperplane exists, the perceptron model will eventually converge to a solution that accurately classifies all the training examples.

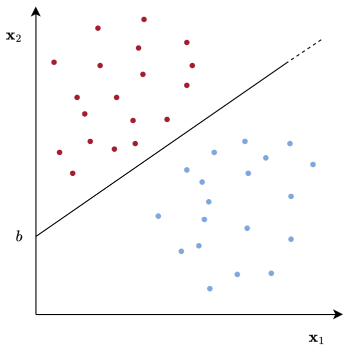

Figure 2.4: An example of a linearly separable problem. In this case, $\mathbf{x}$ has only 2 elements. The perceptron model creates a line (decision boundary) that perfectly separates the examples.

Common examples of linearly separable problems include binary classification tasks, such as distinguishing between spam and non-spam emails or identifying positive versus negative sentiment in text. Additionally, the perceptron can effectively learn certain Boolean functions, like AND and OR, where the output can be separated linearly based on the inputs. Despite its strengths, the perceptron model has

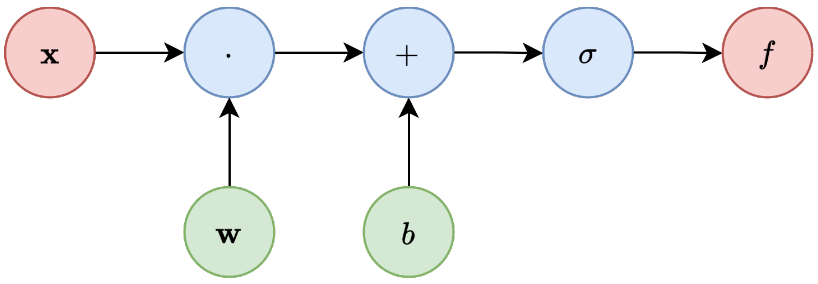

Figure 2.5: Computational graph of a perceptron. Blue nodes represents operators/function, red nodes input/output nodes and green nodes function parameters

notable limitations, particularly when it comes to handling non-linearly separable problems. In cases where no single hyperplane can effectively separate the classes, the perceptron algorithm fails to converge to an accurate solution. A classic example of this limitation is the XOR problem, where the classes are not linearly separable, and thus, the perceptron is unable to find a suitable decision boundary. A graphic example of a non linearly separable problem is depicted in Figure 2.6.

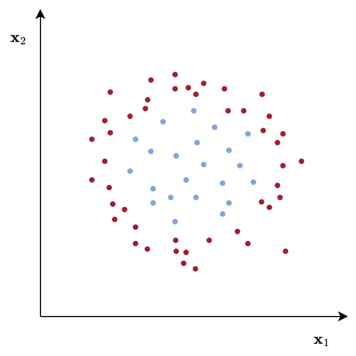

Figure 2.6: An example of a non linearly separable problem. No line can separate clearly the red class from the blue class.

The inability to solve non-linear problems restricts the applicability of the perceptron model to only a subset of classification tasks, a limitation that arises from the linear nature of the decision boundary that the perceptron attempts to establish[16]. Many practical problems exhibit non-linear separability, rendering the perceptron model unsuitable for numerous real-world tasks. Despite the inherent limitations of the perceptron, it serves as a fundamental building block of neural networks. By integrating multiple perceptrons, it is possible to construct a fully connected layer, thereby enhancing the model's capacity to address more complex tasks.

16: The activation field of a perceptron is in fact the expression of a line/plane/hyperplane.

2.2.2 Multi-Layer Perceptron

Using the perceptron as a foundational element, it is possible to construct a more sophisticated and general entity: a fully connected layer. A fully connected layer, also referred to as a network layer, consists of n stacked perceptrons that share the same inputs. As outlined in Equation 2.15, the parameters of this layer are encapsulated within a matrix $\mathbf{W} \in \mathbb{R}^{(n \times m)}$, where n represents the number of perceptrons and m denotes the number of inputs. Each row of the matrix $\mathbf{W}$ corresponds to the weight vector $\mathbf{w}$ of an individual perceptron. Furthermore, the output from this layer is a vector of n elements, with each element reflecting the output from the corresponding perceptron.

$$F(\mathbf{x}; \mathbf{W}) = (f(\mathbf{x}; \mathbf{W}_1), \ldots, f(\mathbf{x}; \mathbf{W}_n)) \tag{2.15}$$

Instead of computing the output of each perceptron indipendently, it is possible to compute the output of all perceptrons of the entire layer in parallel, with just one matrix-vector multiplication as shown in Equation 2.16.

$$F(\mathbf{x};\mathbf{W}) = \sigma\left(\mathbf{W}\cdot\mathbf{x}\right) \tag{2.16}$$

By utilizing this new construct, it is possible to develop arbitrarily powerful models. Each layer, being a function, can be composed with other layers to facilitate sequential computations. In this manner, the output of one layer becomes the input for the next layer, akin to function composition.

$$\mathcal{N}(\mathbf{x};\theta) = (F_1 \circ \cdots \circ F_d)(\mathbf{x}) \tag{2.17}$$

Equation 2.17 formalizes this concept. The resulting model is a fully connected multi-layered neural network with d layers. Each fully connected layer F_i is parametrized by a weight matrix $\mathbf{W}_i \in \theta$, where θ represents the set of all parameters of the model.

All layers between F_i with $i \in 2\ldots d$ are called *hidden layers*.

The models constructed with this framework are called Multilayer Perceptrons (MLP) [18] or Feedfoward Neural Networks (FNN). The main idea of stacking one layer after another in a feedforward network is to enable the model to learn a hierarchical mapping of the data. For example, in the XOR problem, a single-layer perceptron fails because it cannot find a linear boundary to separate the classes. However, by introducing additional layers, each layer can learn to transform the input data into a more suitable representation. The first layer might learn simple features, which are then combined and transformed by subsequent layers into more complex features. This hierarchical learning allows the network to create intermediate representations that progressively disentangle the input data, ultimately enabling the final layer to classify the data accurately. Thus, the network effectively maps the original input space into a new space where the classes become linearly separable.

[18]: Rosenblatt (1959), *Principles of Neurodynamics*

By mapping inputs into diffeerent high-dimensional spaces, FNNs are able to learn effectively any non-linear problem. In fact, it has been proven that any feedforward network composed of two layers can approximate any continuous function on compact subsets of $\mathbb{R}^n$ to arbitrary accuracy, provided it has a sufficient number of neurons and the appropriate activation functions [19]. Feedforward networks are therefore said to be *universal approximators*.

[19]: Leshno et al. (1993), *Multilayer feedforward networks with a nonpolynomial activation function can approximate any function*

2.2.3 Convolutional Networks

While the extreme generality of feedforward models (due to their ability to approximate any function), makes these models very powerful, it also introduces an additional problem. To illustrate this, consider that each model configuration θ of a feedforward network (FFN) represents a point in the high-dimensional space of all possible model configurations called the *hypotheses space*. In this vast configuration space, only a small subspace is relevant for solving the specific problem at hand (i.e., configurations that make the model perform the chosen task). However, as the number of parameters in the network grows, the dimensionality of this space increases, leading to an exponential explosion of possible configurations for the optimization method to explore.

Another problem also arises from the high time and space complexity of gradient computations, which grows linearly with the number of parameters, but the parameters themselves of a feedforward network grow exponentially as the number of neurons increases.

To mitigate this issue, FFNs are deliberately made less powerful by encoding inductive priors into the model. Inductive priors are assumptions about the type of data the model will process and the tasks it must solve. By incorporating these priors, the expressive power of the models is effectively constrained, *limiting* the space of all possible configurations. This confinement helps gradient-based optimization methods focus on regions containing plausible solutions to the problem at hand.

Convolutional Neural Networks (CNNs) [2][20] are a type of neural network architecture that encode specific inductive priors, facilitating the processing of image data. These priors are:

[2]: LeCun et al. (1989), *Handwritten Digit Recognition with a Back-Propagation Network*

- **Locality**: image data consists of pixel values where nearby pixels are more related than distant ones[17].
- **Weight Sharing**: neurons in the same layer share weights, reducing the total number of parameters required for a layer.
- **Pooling**: high-level features (e.g., objects, lines) in an image are meaningful only when interpreted over a sufficiently large patch of pixels.

17: For example, in an image representing a line, pixels will have similar values along the direction of the line.

To encode the first two priors, CNNs utilize a specific type of layer[18] called the *Convolutional Layer*, which is the origin of their name.

18: Recall that layers in neural networks can be seen as the constructs of a differentiable programming language.

Convolutional Layer

Such layer implements a *convolution*, a mathematical operation that (in the discrete case) consists on computing the sum of the product between two functions after one is reflected about the y-axis and shifted.

From Equation 2.18 it can be seen that the convolution actually consists on computing the similarity between two functions, making one of the function to progressively slide over the x dimension.

$$(f \star g)(x) = \sum_{h=-\infty}^{\infty} f(x)g(x-h) \tag{2.18}$$

The convolution layer implements this operation, where f is the input image and g (also called the *kernel*) are the learnable parameters (weights) of the layer. Since images are 2-dimensional bounded discrete functions[19], the operation is applied over both dimensions. Equation 2.19 shows the output of a single convolutional neuron.

$$C(\mathbf{X};\mathbf{W})_{x,y} = \sum_{m=-M/2}^{M/2} \sum_{n=-N/2}^{N/2} \mathbf{X}_{x,y}\mathbf{W}_{(x-m),(y-n)} \tag{2.19}$$

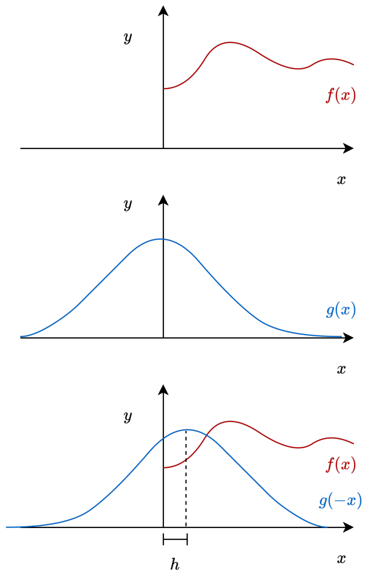

Figure 2.7: Example of the convolution operation in one dimension. Note that in the convolution, g is flipped horizontally ($g(-x)$) and slid over f by a displacement h.

In Equation 2.19, $M \times N$ represents the dimensions of the kernel[20] $\mathbf{W}$ and $\mathbf{X}_{x,y}$ the value of the (x, y) pixel of the input image. Note that since the input is 2-dimensional, even the neurons are arranged in a grid-like manner. That is why each neuron's output is indicized by the variables x and y. The results of the convolutional layer is then also a matrix, called *feature map*. From Equation 2.19 it is also clear how the locality prior is effectively encoded: each neuron process only a subset of the input[21]. The second prior is explained by the fact that each value of $\mathbf{W}$ is shared between each neuron. That is, for a single convolutional layer, there exists only an $M \times N$[22] matrix of parameters, which, as previously mentioned, is much smaller than the input size. The number of parameters of a convolutional layer is therefore much smaller than its fully connected counterpart.

19: Images can be seen as the the sampled version of a 2-dimensional real valued signal

20: Which are typically much smaller than the input image size.

21: That corresponds to a window with dimension $M \times N$, centered at the (x, y) position.

22: Without counting other factors such as the sliding window and the number of channels.

To be precise, image data is composed of multiple channels which are commonly 3: red, green and blue. The extension for the convolution layer is straightforward, it is sufficient to apply the convolution on an additional dimension which represent the channel, thus, for RGB images, convolutional filters are typically matrices with dimensions $M \times N \times 3$, where 3 is the number of channels.

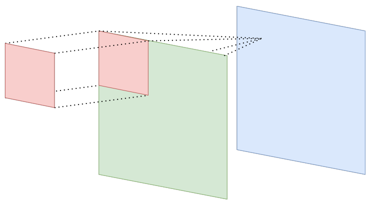
Figure 2.8: In the convolution operation the kernel (red square) is applied over the image (green square) to produce the corresponding value on the feature map (blue square). To compute the next value, the kernel is then slid by a number of positions determined by the *stride*.

To intuitively comprehend the application of a convolution over a two-dimensional image, one can visualize it as applying a patch (kernel) of $M \times N$ elements over the image and computing its weighted sum. This process involves sliding the patch across all values of the image, with the step size, known as the *stride*, determining the movement of the kernel to subsequent positions. In scenarios involving multiple channels, the operation is performed by applying each patch with identical dimensions to each channel independently and in parallel. To manage data at the edges of the image, zero padding is typically applied to the original image, ensuring that the convolution process can address corner data without loss.

Pooling Layer

The pooling prior is encoded by the *pooling layer*. This layer performs a down-sampling of the input signal, utilizing a sliding window approach similar to the convolution operation discussed previously. Various down-sampling methods can be employed, but this discussion focuses on the most commonly implemented strategies in pooling layers. Equation 2.20 illustrates the output of an average pooling neuron and a max-pooling neuron, respectively, applied to an $M \times N$ window[23].

23: Typical window sizes for pooling layers are 2×2 and 3×3.

$$\begin{aligned} P^{avg}(\mathbf{X})_{x,y} &= \frac{1}{L \cdot K} \sum_{l=-L/2}^{L/2} \sum_{k=-K/2}^{K/2} \mathbf{X}_{x-l,y-k} \\ P^{max}(\mathbf{X})_{x,y} &= \max_{\substack{l \in -L/2,\ldots,L/2 \\ k \in -K/2,\ldots,K/2}} \mathbf{X}_{x-l,y-k} \end{aligned} \tag{2.20}$$

Just as the convolution, this process is applied in a sliding window manner. It follows that the considerations regarding edge handling and striding made previously are valid for this layer as well. Another important consideration regarding the pooling layer is that it does not contain any learnable parameters, which significantly reduces the computational complexity of the model.

Network Architecture

Having discussed the fundamental building blocks of convolutional networks, the focus now shifts to the actual model architecture, specifically how these blocks are arranged to construct a model. Typical convolutional neural network architectures consist of two main components: a feature extractor and a fully connected head. The feature extractor comprises a series of convolutional and pooling layers. The rationale behind this structure is that convolutional layers, through the application of filters to the input image, generate feature maps that emphasize various image aspects, such as edges, textures, and complex patterns. Conversely, pooling layers select the most significant features by down-sampling the input, thereby reducing the spatial dimensions of the feature maps. The sequential application of these operations progressively transforms the input data into smaller feature maps that capture increasingly abstract information about the image[24].

24: For example, initial convolutional layers might detect simple features such as edges and corners, while deeper layers might recognize more complex structures like shapes and objects.

The feature extractor is also referred to as the *encoder* because it encodes the image data into a compact representation containing all the salient features necessary to solve the task for which the network has been optimized. Consider, for instance, a CNN that processes input images with three channels (RGB) and dimensions $W \times H$. Through the progressive application of convolution and pooling layers, the final feature map (the output of the encoder) might have dimensions of 8×8. The output of the model is often *flattened*, meaning it is reshaped into a one-dimensional vector, resulting in an output of 64 features. Consequently, the encoder part of the network can be viewed as a mapping $\mathbb{R}^{W \times H \times 3} \rightarrow \mathbb{R}^{64}$. This 64-dimensional space is called the *latent space* because the vectors in this space contain *latent* (hidden) features that the model has learned during training. The encoding part of the model serves to extract all salient features from the image, progressively selecting them until a compact representation of the input is obtained. This representation is then fed into the second part of the model: a fully connected neural network, which performs the actual task, such as image classification.

Due to the reduced number of parameters in convolutional layers, CNNs can scale up with a significantly larger number of layers while maintaining manageable computational com-

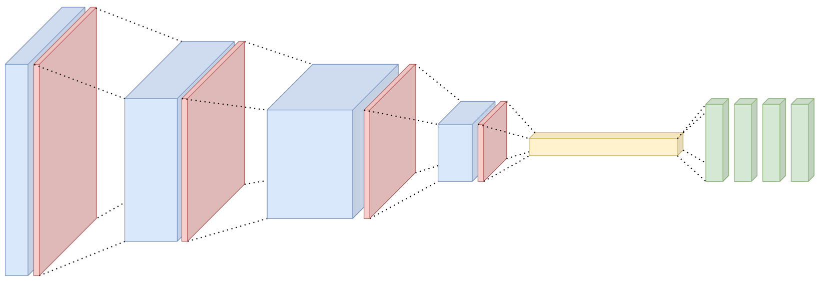

Figure 2.9: Graphical depiction of Convolutional Neural Network Architecture. In blue are represented convolutional layers. Their depth is proportional to the number of filters applied in parallel by the layer. In red are depicted the pooling layers, while in green the fully connected layers. The yellow block represents the hidden representation, that is, the flattened vector that represents the encoder's output.

plexity. Although all convolutional networks follow a similar structure, they vary in the number and types of layers, as well as in their hyper-parameters. Extensive research has been dedicated to identifying the optimal convolutional network architecture, focusing on the most effective number and configuration of convolutional, pooling, and fully connected layers. Table 2.3 summarizes some of the most prominent convolutional architectures found in the literature, along with their total number of parameters.

Architecture	Parameters
AlexNet [21]	60M
VGG-16 [22]	138M
ResNet18 [23]	11.4M
DenseNet100 [24]	0.8M

Table 2.3: Common convolutional network architectures, along with their total number of parameters. The architectures are arranged chronologically from older to more modern designs. It is noteworthy how the number of parameters has decreased over the years, attributed to the development of more efficient techniques, which are beyond the scope of this discussion.

During this work, the ResNet [23] architecture has been predominantly employed, as will be further discussed in Chapter 4. Therefore, it is worth to briefly discus its details here.

[23]: He et al. (2016), *Deep Residual Learning for Image Recognition*

ResNet

To understand the rationale behind the ResNet architecture, it is crucial to first comprehend the vanishing gradient problem. As discussed previously, gradient-based optimization methods function by calculating the gradient of the loss with respect to the model's parameters. These gradients are computed using an algorithm that applies the chain rule, multiplying the gradients at each intermediate computational step. However, a challenge arises when the gradients from these intermediate steps are small. As these gradients are propagated back toward the input layers, they can become progressively diminished. This leads to the vanishing gradient problem, where early layers receive an increasingly smaller gradient signal, effectively stalling the training of the model as these layers learn very slowly or not at all. This poses a significant challenge for the training of deeper networks, as the vanishing gradient problem becomes more pronounced with an increase in the number of layers[25]. However, He et

25: This is due to the proportional increase in the number of dilution steps through which the gradient must pass.

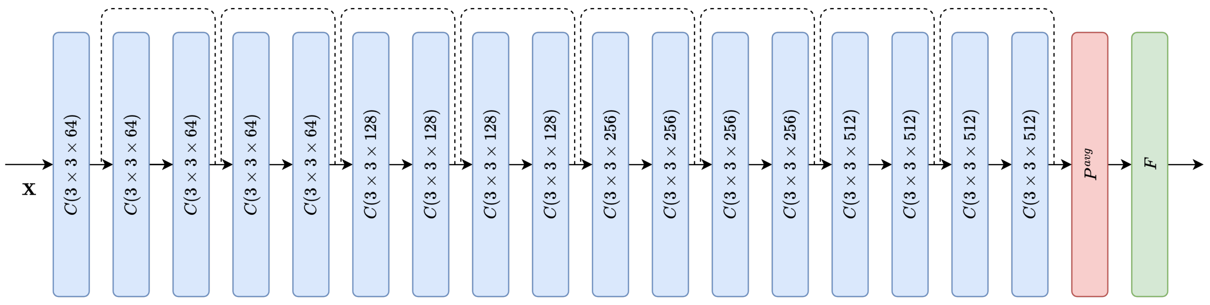

Figure 2.10: Graphical depiction of the ResNet-18 architecture. The residual connections between layers are depicted in dashed lines. Each convolutional block, depicted in blue, is labeled with its dimensions $W \times H \times C$, representing width, height, and channel count, respectively.

al. [23] demonstrated that using a special type of connection, known as *residual connections*, can effectively mitigate this issue. Residual connections allow gradients to flow directly through the network by skipping layers. By introducing a shortcut path that bypasses the non-linear transformations, the network can learn identity functions where necessary, ensuring that the signal is not diluted through deep layers. This approach has significantly facilitated the training of deeper networks, as it provides a way for the gradient to pass through without being dampened by multiple layers of data transformation.

The set of layers that are bypassed by the residual connection is known as a *residual block*. The skip connection within these blocks is straightforwardly implemented by summing the input of a residual block to its output. ResNet incorporates these fundamental units, each comprising convolutional layers. In the original paper by He et al. [23], the authors propose different versions of this architecture, reflecting various sizes and depths. In this thesis, the primary focus has been on employing the ResNet-18 architecture, a variant of the ResNet family that consists of 18 layers. This architecture adheres to the typical design principles of convolutional networks but incorporates residual connections between layers to enhance learning in deeper networks. Figure 2.10 provides a detailed illustration of the ResNet-18 architecture.

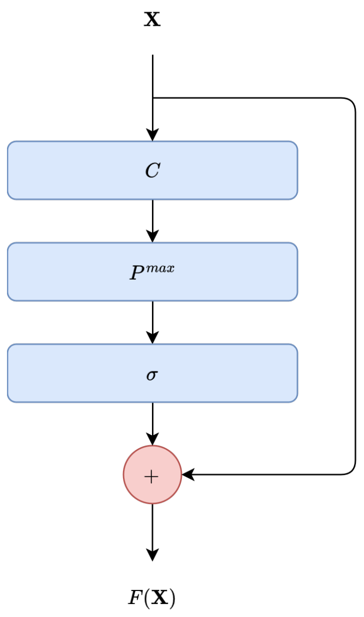

Figure 2.11: A residual block composed of a convolutional layer C, max pooling layer P^{max} and an activation function σ. The residual connection connects the input $\mathbf{X}$ of the residual block to its output $F(\mathbf{X})$ by summing them together. In other words, the output of this residual block can be represented as $F(\mathbf{X}) = (C \circ P^{max} \circ \sigma)(\mathbf{X}) + \mathbf{X}$.

Neuroimaging 3

Neuroimaging serves as a powerful tool for the non-invasive examination of in vivo brain structure and function, offering critical insights into brain operations and the genesis of various conditions. Magnetic Resonance Imaging (MRI) stands out among diverse imaging techniques for its ability to produce high-resolution images without employing ionizing radiation, rendering it invaluable in both clinical settings and research applications. This chapter provides an overview of the main neuroimaging techniques, with a particular emphasis on MRI and T1-weighted imaging. The chapter begins by outlining the principal acquisition methods foundational to neuroimaging, highlighting how each technique captures unique aspects of brain anatomy and function. The focus then shifts to the various MRI modalities, with a particular focus on the characteristics and applications of T1-weighted imaging, which is renowned for its effectiveness in delineating the brain's anatomical structures. The discussion then progresses to processing methods typical in neuroimaging, focusing particularly on Voxel-Based Morphometry (VBM), an advanced analytical technique that enables detailed structural analysis of the brain through statistical means. Lastly, this chapter presents brain parcellation techniques crucial for segmenting the brain into distinct anatomical regions. Particular attention is given to the Desikan et al. [25] atlas, a widely utilized parcellation scheme in this thesis.

3.1 Acquisition Methods

In neuroimaging, a variety of acquisition technologies are employed, each tailored to capture distinct aspects of brain structure and function. Below is a general overview of several key neuroimaging acquisition techniques:

- **Structural Magnetic Resonance Imaging (sMRI)**: uses magnetic fields and radio waves to generate detailed images of the brain. MRI can be tailored to highlight various tissue properties and includes several specific types that will be discussed further on.

- **Functional Magnetic Resonance Imaging (fMRI)**: uses magnetic fields to measure brain activity by means of changes associated with blood. flow[1]. fMRI can be used to observe neural activity and to define functional anatomy of the brain.

1: When an area of the brain is in use, blood flow to that region also increases.

- **Diffusion Magnetic Resonance Imaging (dMRI)**: leverages the magnetic properties of water molecules to map the diffusion of water present in the brain's white matter. This acquisition method help in visualizing and analyzing the brain's white matter tracts, providing insights into the brain's connectivity and structural integrity.
- **Computed Tomography (CT)**: uses X-rays to create detailed images of the brain. Particularly useful for quickly detecting injuries, bleeding, tumors, and other structural abnormalities.
- **Positron Emission Tomography (PET)**: uses radioactive tracers to observe metabolic processes in the brain. PET is highly effective for studying brain metabolism and blood flow, and is often used in research on neurological and psychiatric conditions.
- **Single Photon Emission Computed Tomography (SPECT)**: similar to PET, SPECT uses radioactive tracers and a gamma camera to detect cerebral blood flow and brain activity functional changes.
- **Electroencephalography (EEG)**: uses electrodes placed along the scalp to detect electrical activity in the brain. EEG is particularly valuable for diagnosing conditions like epilepsy and sleep disorders, and for research on brain states such as alertness or sleep.
- **Magnetoencephalography (MEG)**: records magnetic fields produced by neural activity, offering a direct measurement of brain activity. MEG is used to study cognitive functions, neural responses, and to map brain functions.

It's important to note that this list of neuroimaging acquisition technologies is not exhaustive. There are additional methods and variations within each category that may be used depending on specific diagnostic or research needs. Each technology offers distinct advantages for exploring different facets of brain structure and function, but it is beyond the scope of this work to discuss all of them in detail. This thesis will specifically focus on Deep Learning techniques applied to Magnetic Resonance Imaging (MRI), and thus the discussion will now shift to this neuroimaging modality in particular.

3.2 Magnetic Resonance Imaging (MRI)

An MRI scanner primarily functions as a large magnet that creates a constant magnetic field strength (B_0) when activated [26]. During an MRI scan, a patient is positioned within the scanner's bore, and the hydrogen protons (H_1) within the patient's body are exposed to this static magnetic field. This exposure causes the protons' spins to precess[2] around the B_0 direction. To manipulate these spins, Radiofrequency (RF) excitation pulses are directed to the head or a specific body section through either a single transmission coil or an array of them. These RF pulses align the proton spins within the targeted area to the direction of the RF pulses.

[26]: Grover et al. (2015), *Magnetic Resonance Imaging: Principles and Techniques: Lessons for Clinicians*

2: Precession is a change in the orientation of the rotational axis of a rotating body.

Once the RF pulses cease, the aligned spins begin to relax back to their initial states. This relaxation process varies based on the surrounding environment and the magnetic resonance (MR) relaxation properties of different tissue types within the body. The energy released during this relaxation is captured by one or more receiver coils, translating it into a raw data matrix known as *k-space*. As a final step, this data undergoes a series of signal-processing techniques that transforms this raw data into the MR images that are then used for clinical assessment or research. MR images are composed of digital image voxels, which are essentially 3D volumes, in contrast to pixels that represent 2D squares. Each voxel in an MR image contains a signal that represents all the MR-visible protons within that specific volume. This setup allows for a three-dimensional representation of the scanned area, providing depth that a two-dimensional pixel-based image cannot.

Higher magnetic field strengths in MR scanners enhance the quality of these images. The stronger the magnetic field (B_0), the greater the level of detail that can be achieved. This is because higher field strengths improve the signal-to-noise ratio and the resolution of the images, allowing for better differentiation of tissue types and more precise imaging of fine structures. Consequently, MR scanners with higher field strengths are capable of producing images with better clarity and more distinct separation of signals[3]

3: For instance, MRI scanners commonly found in hospitals utilize magnetic field strengths of either 1.5 Tesla or 3 Tesla.

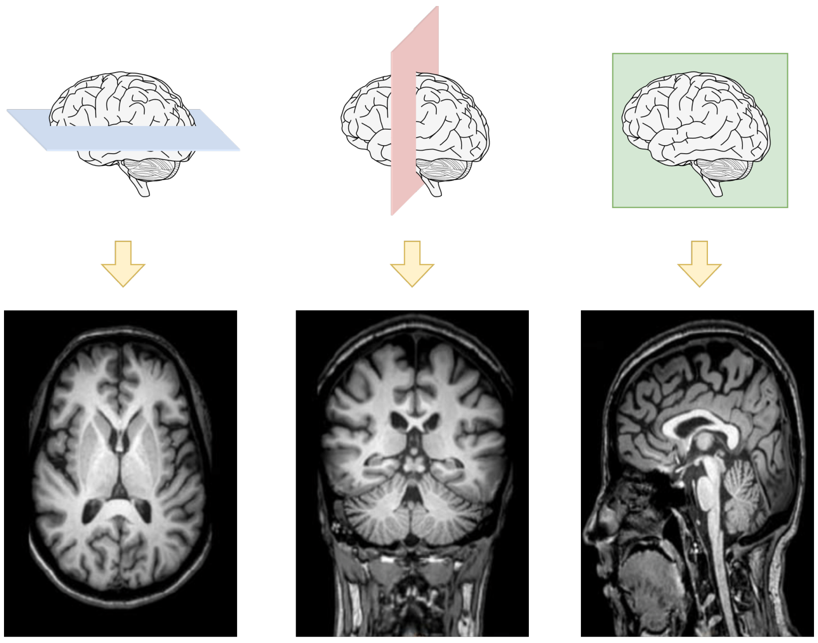

Figure 3.1: An MRI scan captures images of the brain from three different planes: axial, coronal, and sagittal. This figure shows the acquisition planes along with their corresponding generated images. The axial plane is depicted in blue, the coronal plane in red, and the sagittal plane in green.

As mentioned earlier, each tissue type responds uniquely to the magnetic pulses used in MR imaging. This differential response is precisely what the so called T1 and T2 weighting exploit to enhance the visibility of various tissues within the magnetic resonance images.

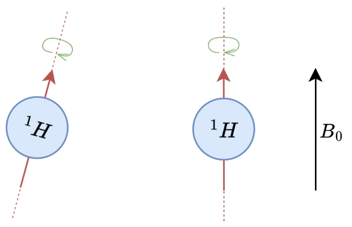

Figure 3.2: Hydrogen atoms spin along their axis. When a magnetic force is applied (B_0) their rotational axis is pulled towards the direction of the magnetic field.

T1-weighted imaging capitalizes on the *longitudinal relaxation time* (T_1), which is the time it takes for protons to realign with the magnetic field B_0 after the removal of the RF pulse. T1 times vary between different types of tissue; for instance, fat has a shorter T1 time compared to water. In T1-weighted images, tissues with shorter T1 relaxation times appear brighter. Thus, these images are particularly effective for visualizing the anatomy of the brain, distinguishing between grey and white matter, and identifying fatty tissues, making them valuable for detailed anatomical studies.

T2-weighted imaging, on the other hand, emphasizes the *transverse relaxation time* (T_2), which is the time it takes for protons to lose phase coherence among the directions perpendicular to the magnetic field, primarily due to interactions with neighboring molecules. Tissues with longer T2 times, such as fluids, appear brighter on T2-weighted images. This characteristic makes T2-weighted imaging exceptionally useful for detecting fluid-filled areas, such as edema, tumors, and inflammation in tissues.

The choice between T1 and T2 weighting depends on the diagnostic requirements; T1 is preferred for detailed anatomical definition, while T2 is superior for identifying fluid changes. This flexibility is a key strength of MRI technology, allowing for tailored imaging that aligns closely with clinical and research needs. In this work, the datasets used contained predominantly T1-weighted images.

3.3 Voxel Based Morphometry

Following the acquisition phase, MRI images can undergo analysis either automatically (e.g., by a machine learning model) or manually. Nonetheless, several inherent challenges may compromise the reliability of the data, especially when comparing images across different individuals. Each individual's brain presents distinct anatomical characteristics, including variations in size, shape, and the distribution of tissues such as gray matter (GM), white matter (WM), and cerebrospinal fluid (CSF). These discrepancies complicate direct comparisons between scans because corresponding brain regions may not align precisely across different individuals. This variability also impedes the ability to draw comparisons or discern trends across populations or patient groups[4]. Additionally, MRI scans are prone to various types of noise and artifacts, which may originate from the scanner, environmental conditions, or subject-related factors such as minor movements during scanning. These extraneous signals can mask essential details critical for precise diagnosis or effective research analysis.

4: Coincidently, a task that must be performed by Neural Networks.

To address these challenges, a pre-processing technique called Voxel-Based Morphometry (VBM) [27] has been developed. VBM standardizes and simplifies the process of comparing brain anatomy across different individuals by focusing on measuring differences in the composition of brain tissue, specifically the concentration and volume of gray and white matter. The concept of VBM comprises three basic preprocessing steps: (1) *spatial normalization*, (2) *tissue segmentation* , and (3) *spatial smoothing*, which are followed by the actual statistical analysis.

[27]: Ashburner et al. (2000), *Voxel-Based Morphometry—The Methods*

In the spatial normalization step, the MRI scans are matched together spatially (registered) so that a location in one subject's MRI corresponds to the same location in another subject's MRI. It is generally achieved by registering all images from a study onto the same template image[5] so that they

5: A common template frequently used in the literature is the MNI (Montreal Neurological Institute) template [28], which has also been utilized in this study.

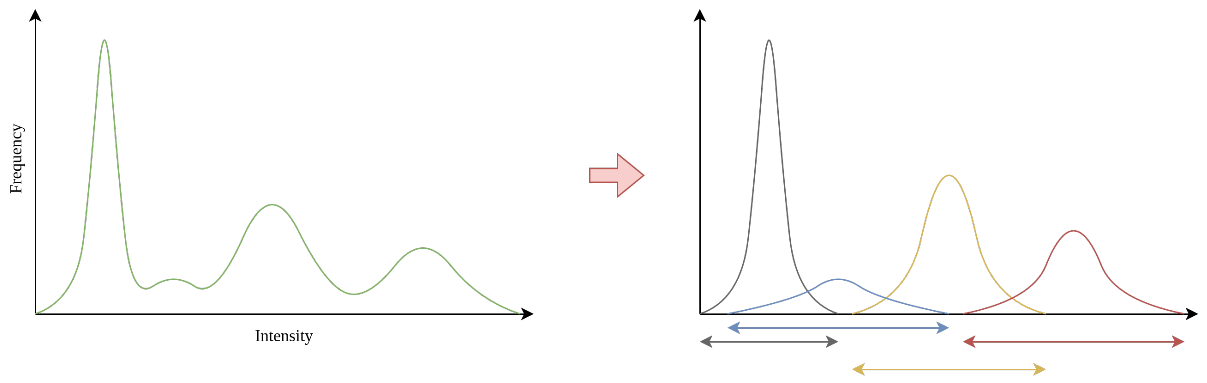

Figure 3.3: On the left, an hypothetical distribution of intensity values of an MRI image. When this image undergoes tissue segmentation, the original distribution of intensity values is segmented into different distributions that represent a specific tissue class (right figure). For example, the gray one may represent background, the blue cerebrospinal fluid, the yellow white matter and the red grey matter. Note that in this case tissue-specific intensity distributions overlap. This is due to the fact that each voxel can contain more than one tissue.

are all in the same space. The template image could be one specific MRI scan or could be created by averaging across a number of different MRI scans that have been put in the same space. After the template image has been obtained, either linear or non linear transformations can be used to perform this registration [29].

[29]: Kurth et al. (2015), *Voxel-Based Morphometry*

The tissue segmentation process is the subsequent step, which involves partitioning the MRI images into different tissue compartments such as white matter (WM), gray matter (GM), and cerebrospinal fluid (CSF). As previously discussed, in T1-weighted images (which are the focus of this thesis) the longitudinal relaxation time (T_1) varies across different types of tissue. Consequently, each tissue type displays a distinct level of brightness in the images. This difference allows for the assignment of specific tissue types based on their brightness levels. Essentially, this phase involves creating a map of brightness values that correspond to different tissue types, enabling the accurate identification of each tissue within the MRI images. To construct such a map, the distribution of intensity values within the MRI images is divided into several smaller distributions, each representing a specific tissue class. In practice, each voxel, commonly measuring $1mm$ isotropic, may contain multiple tissue types, causing overlaps between the intensity distributions of different tissue classes. This overlap can result in voxels being classified under more than one tissue category.

To address this challenge, tissue segmentation can be enhanced with the use of additional probability maps that incorporate prior knowledge about the typical locations of different tissues within the brain [30]. For each tissue type, a probability map is used that indicates how likely a particular voxel is to represent that tissue. This probabilistic approach helps to refine the decisions made by the tissue classification algorithm, ensuring a more accurate segmentation. Since the algorithm uses a probabilistic approach, the result is an estimation of tissue composition for each voxel in the image.

[30]: Ashburner et al. (2005), *Unified segmentation*

The third and last step consist of a spatial smoothing, which consist on the application of a convolution operation with a Gaussian filter[6]. The first is that smoothing can improve effectively the signal-to-noise ratio by averaging the intensities of neighboring voxels. This reduction in noise is essential because it helps to reveal the true anatomical differences underlying the images, minimizing the impact of random fluctuations that might otherwise be mistaken for significant variations.

6: A Gaussian Filter is a kernel whose values are sampled from a Gaussian distribution. In this case, they are sampled from a 3-dimensional Gaussian distribution.

Moreover, smoothing serves to increase the statistical power of the analyses conducted in VBM. By making the data more normally distributed across voxels, smoothing aligns with the statistical assumptions required for many of the inferential techniques used in neuroimaging studies. This alignment is crucial as it not only validates the use of parametric statistical tests but also enhances the reliability of the findings by increasing the effective sample size at each voxel. This approach provides a more robust basis for detecting differences that are statistically significant rather than those arising from the noise. Another key aspect of smoothing is its ability to account for minor registration errors between subjects' images. Despite the application of the spatial normalization step, slight misalignments can still occur due to the inherent variability in brain anatomy among individuals. Smoothing helps to mitigate these differences by blurring sharp edges and increasing the overlap of similar anatomical structures across different scans. This adjustment is particularly beneficial for ensuring accurate comparisons are made in studies comparing groups of subjects, as it helps ensure that equivalent anatomical regions are analyzed across all images.

Furthermore, smoothing is instrumental in matching the voxel-wise data to the assumptions of Gaussian field theory, which underpins many of the statistical methods used to

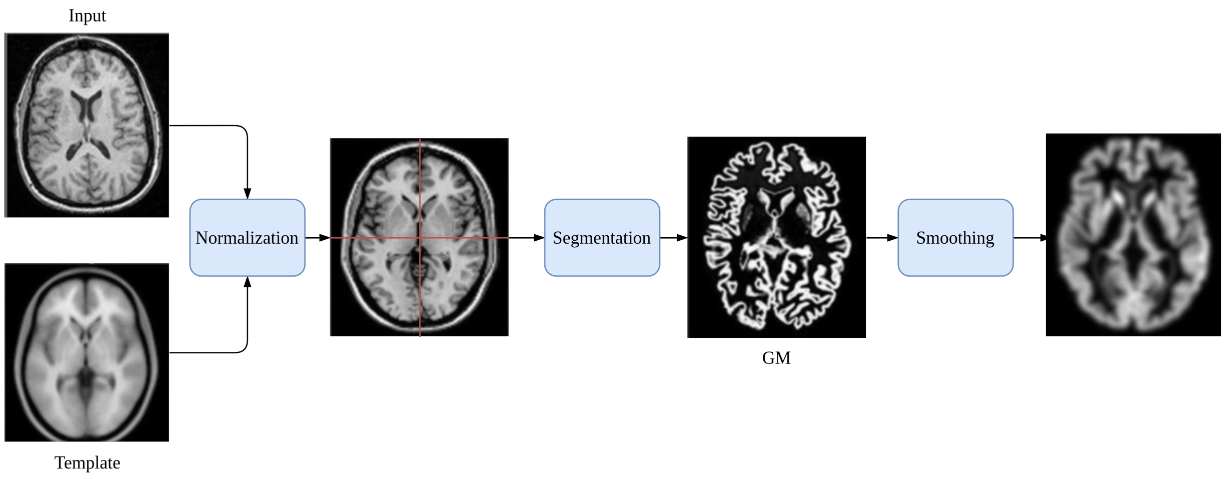

Figure 3.4: VBM processing is conducted in three steps. Initially, normalization is applied to all images using a standard template to ensure that they are aligned to the same frame of reference. The second step involves segmenting the normalized images into different tissue types, identifiable by their distinct intensity values. This segmentation results in the creation of separate volumes for each tissue type; for illustrative simplicity, only Gray Matter is depicted in this figure. The final step in the VBM process is the application of Gaussian smoothing to each of these segmented volumes.

draw inferences from neuroimaging data. This theory relies on the smoothness of the data to make valid statistical claims about the presence of significant brain regions. By applying a Gaussian filter, the data better approximate a continuous Gaussian field, thus fulfilling the theoretical prerequisites necessary for accurate *p-value* calculation and hypothesis testing.

Today there are various tools that perform VBM pre-processing, each with its own choice for the implementations of the aforementioned steps. For the pre-processing of MRI images used in this work, the BrainPrep [31] software has been used, which is based on two common pre-processing packages in neuroimaging CAT12 [32] and FreeSurfer [33].

3.4 Brain Parcellations

Brain parcellation is a method utilized in neuroimaging to divide the brain into distinct regions based on anatomical landmarks, functional specialization, or connectivity patterns. This technique is crucial for reducing the complexity of the brain's architecture into manageable segments, thereby enabling more focused and detailed analyses of its structure and function. Particularly in anatomical MRI, parcellation proves invaluable for isolating specific areas of interest to evaluate their individual contributions to overall brain anatomy. The significance of brain parcellation stems from its ability to enhance understanding of the relationships and interactions among various parts of the brain. Segmenting the brain into regions allows to effectively correlate specific structural changes with cognitive functions or pathological states, facilitating deeper insights into brain functionality and disorder.

The terms *parcellation*, *atlas*, and *template* are often used interchangeably in the literature.

Brain parcellations not only provide insights into the organizational principles of the human brain but also offer significant practical benefits as biologically informed strategies for data reduction. This process allows the information from hundreds of thousands of voxels in MRI images to be compressed into a manageable set of regions that reflect distinct entities [34]. Such reduction is crucial, particularly for neural network models, which can utilize this streamlined data to predict behavioral or clinical phenotypes from brain imaging data. However, for this aggregation to serve as a valid form of data compression, the delineated parcels must represent a biologically meaningful patterning.

[34]: Eickhoff et al. (2018), *Imaging-based parcellations of the human brain*

Over the past two decades, a variety of reliable brain parcellations have been developed, each exhibiting specific strengths and weaknesses. These parcellations have become essential tools for the analysis of neuroimaging datasets. Depending on the type of data they utilize, and consequently the acquisition method employed, these methods can be classified into three broad categories [35]:

[35]: Moghimi et al. (2021), *A Review on MR Based Human Brain Parcellation Methods*

- Anatomical parcellations, which are constructed from T1-weighted MRI images.
- Functional parcellations, derived from from functional MRI (fMRI) images.
- Structural parcellations, based on diffusion-weighted-imaging data.

This thesis will specifically focus on anatomical parcellations. Within this context, each defined region, known as a *Region of Interest (ROI)*, is assigned a specific label. As noted earlier, T1-weighted MRI images effectively capture the anatomical structure of the brain. This includes the intricate folding patterns of the cortical surface (its *sulci* and *gyri*[7]) as well as sub-cortical structures[8].

7: The cortical surface is the outer layer of neural tissue of the brain. Sulci and gyri are the characteristic folds and ridges of the brain, respectively.

8: Unlike cortical structures, sub-cortical structures are anatomical features located beneath the cortical surface.

A prevalent method for constructing anatomical parcellations involves using gyri and sulci as markers to delineate the boundaries of regions of interest. The brain displays prominent sulci that typically demarcate each functional area, and by examining these major sulci, one can determine the boundaries of each ROI. The process for identifying the landmarks used to define each ROI, along with the number of ROIs, is encapsulated in a set of guidelines utilized by neuroanatomy experts to manually label the MRI images.

Given a specific set of guidelines, there are multiple methods for parcellating new brain images. The approach discussed later in this thesis primarily involves registering a new brain image to a template image that has already been manually parcellated; this template is referred to as the *reference atlas*. Typically, a reference atlas is constructed from a collection of brain images that have been manually segmented according to established guidelines. Once the reference atlas is prepared, it facilitates the automatic parcellation of new images.

Each atlas proposed in the literature adheres to a specific set of guidelines, which results in variations in the number and delineation of Regions of Interest (ROIs). This thesis will focus on two major atlases: the Desikan-Killiany Atlas [25], which has been predominantly utilized in this research, and the Destrieux Atlas [36]. These atlases exemplify how differing guidelines can influence the definition and segmentation of brain regions, impacting the analysis and interpretation of neuroimaging data.

[36]: Destrieux et al. (2010), *Automatic parcellation of human cortical gyri and sulci using standard anatomical nomenclature*

3.4.1 Desikan-Killiany

The Desikan-Killiany parcellation scheme divides the cortical area of the brain into 34 regions of interest per hemisphere, resulting in a total of 68 ROIs for the entire brain. To develop the Desikan atlas, the authors utilized a dataset of 40 MRI scans that had been manually labeled by neuroanatomy experts. Various sources of information were utilized to delineate the number of ROIs and their anatomical boundaries, wich are discussed extensively in the original publication [25] and are beyond the scope of this discussion.

An automated algorithm, guided by the reference atlas, can subsequently be applied to each new MRI scan to generate its corresponding parcellation. In their foundational study, the authors compared a series of automatically parcellated brains

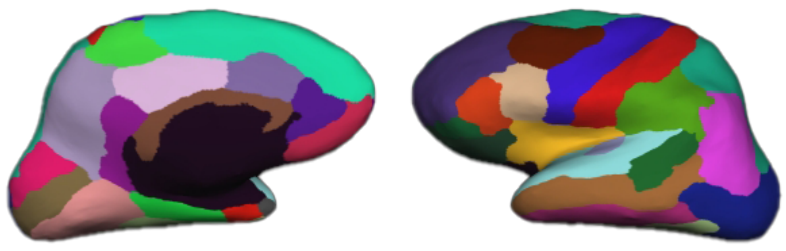

Figure 3.5: Desikan Atlas. Each different color corresponds to a specific region of interest.

with manually parcellated counterparts. The results demonstrated sufficient precision to affirm the method's anatomical validity and reliability, indicating that this automated approach is both effective and dependable for replicating established neuroanatomical segmentations.

Each ROI within the Desikan scheme is characterized by a vector of different anatomical measures, calculated over the corresponding volume represented by the ROI. The selection of features depends on the image analysis software employed. In this instance, the analysis software utilized [33] encompasses seven anatomical measures. These measures provide a summary of various structural aspects of the brain regions, which include:

[33]: Fischl (2012), *FreeSurfer*

- **Average Cortical Thickness**: measures the average thickness of the cerebral cortex across the corresponding ROI.
- **Standard Deviation of Cortical Thickness**: measures the variability in terms of standard deviation of the cortical thickness within the ROI.
- **Gray Matter Volume**: quantifies the total volume of gray matter within the specified parcellated region.
- **Total Surface Area**: calculates the overall area of the cortical surface within each segmented region, relating to the extent of cortical folding.
- **Integrated Mean Curvature**: a differential geometry measure that computes the curvature of a surface by averaging the maximum and minimum curvatures registered across the ROI.
- **Gaussian Curvature**: similar to the Integrated Mean Curvature, but calculates the global curvature as the product of the minimum and maximum curvatures.
- **Intrinsic Curvature Index**: another measure to define

global curvature, dependent on the distance between the highest and lowest curvatures of the surface.

Following this discussion, the Desikan parcellation process outputs a corresponding matrix $\mathcal{D} \in \mathbb{R}^{68\times7}$, where each row contains the discussed measures of a specific region of interest. This matrix can be leveraged by deep learning models as additional data during the training phase (as discussed in Chapter 4) or as an alternative imaging format.

3.4.2 Destrieux

As previously noted, each anatomical atlas is distinctly shaped by the set of guidelines that determine the number, position, and delineation of Regions of Interest (ROIs). In the case of the Destrieux atlas, the guidelines were derived from classical anatomical nomenclature as documented by Duvernoy [37]. These rules were meticulously applied to manually label each of twelve brains. The data from these manually parcellated brains were subsequently utilized as a training set for a statistical algorithm, which was employed to create the final Destrieux reference atlas. The resulting atlas comprises 74 regions of interest for each brain hemisphere, culminating in a total of 148 ROIs. Despite these differences from other atlases, the Destrieux atlas retains the same anatomical measures for each ROI. Consequently, a Destrieux atlas for a particular brain can be systematically represented in a matrix format, $\mathcal{D} \in \mathbb{R}^{148\times7}$, where each row corresponds to an ROI and each column to one of seven the anatomical measures.

[37]: Duvernoy et al. (1999), *The Human Brain: Surface, Three-Dimensional Sectional Anatomy with MRI, and Blood Supply*

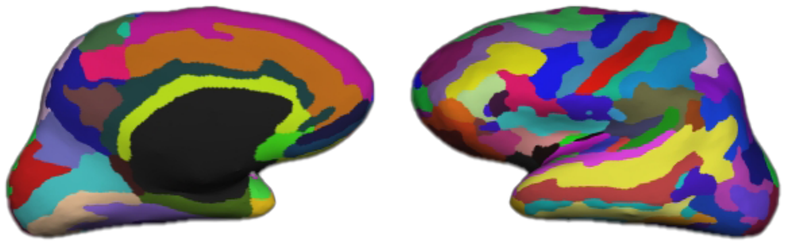

Figure 3.6: Destrieux Atlas. Each different color corresponds to a specific region of interest.

Anatomical Contrastive Learning 4

This chapter will discuss the proposed method that is the subject of this thesis. To set the stage for the discussion, common approaches in deep learning applied to neuroimaging and related state-of-the-art works will be reviewed. Following this, the discussion will shift to an explanation of the various steps and attempts made to extend existing SOTA approaches, ultimately leading to the final formulation. Furthermore, the results of the conducted experiments will be discussed.

4.1 Related Works

Until now, the discussion has primarily focused on the supervised framework of machine learning. In this framework, as previously explained, the model learns by using a discriminator (a class label) applied to the data. This approach is particularly effective when large labeled datasets are available. Deep convolutional models, for instance, require a substantial amount of data to learn salient features and regularities within the data, especially pertinent to brain disorders, which involve clinical, biological, and environmental factors.

However, the availability of large-scale labeled datasets poses a significant challenge, particularly in the medical field [38]. Neuroimaging datasets, for example, typically range from a few hundred to a few thousand participants, which is considerably smaller compared to the datasets used for training state-of-the-art classification models[1]. This limitation becomes even more pronounced for neuroimaging datasets pertaining to specific rare disorders.

[38]: Lan et al. (2020), *Generative Adversarial Networks and Its Applications in Biomedical Informatics*

1: For instance, ImageNet [39] contains more than 14 million images.

4.1.1 Transfer Learning

Transfer learning has demonstrated to be a powerful tool to overcome these limitations in the neuroimaging domain, outperforming standard machine learning approaches in major tasks related to clinical psychiatry [40]. Instead of directly

[40]: Dufumier et al. (2024), *Exploring the potential of representation and transfer learning for anatomical neuroimaging: Application to psychiatry*

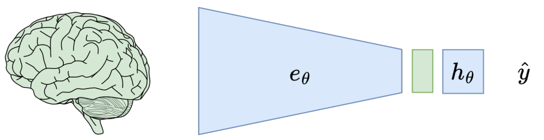

(a) In the brain age prediction settings, the encoder e_θ learns a latent representation of the image data that is then used by a discriminator h_θ to predict the age. The predicted age $\hat{y}$ is then confronted with the real age y in an appropriate loss function.

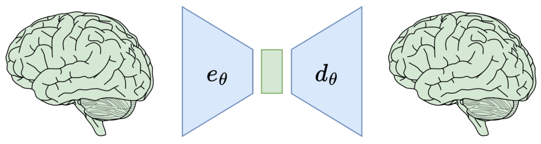

(b) Variational Autoencoders consist of an encoder e_θ that compresses input data into a latent space representation (green block) and a decoder d_θ that reconstructs the input data from these encoded representations. In other words, the decoder learns to map the latent space back to the original data distribution.

learning from a small labeled dataset in a supervised manner, the transfer learning paradigm employs a two-phased approach. In the first phase, the model f_θ is trained on a substantial set of image data of healthy controls[2]. During this phase, the CNN model is trained to learn a low-dimensional embedding space discovering the general variability associated with non-specific variables such as, for example, age and sex. The feature extractor can learn to identify various brain features from the image data present in the dataset. The result of this process is the set of pre-trained weights θ_{HC} of the model on the healthy control data. In the literature of neuroimaging, the pre-training phase has been implemented in several ways:

2: Healthy controls are individuals who do not have the condition or disease being studied and are used as a standard or baseline for comparison against those who do have the condition, to identify differences related to the disease.

- **Contrastive Learning**: this method involves minimizing the distance between encoded representations[3] of same-class pairs while maximizing the distance between representations of different-class pairs. Classes are determined based on the sample label.
- **Autoregressive Learning**: a Variational AutoEncoder (VAE) (Figure 4.1a) is trained to regenerate the same input image. Subsequently, the encoder's weights from the learned VAE are utilized as the feature extractor's weights in the pre-trained model.
- **Brain Age Prediction**: when data associated with the age of the patient is available, the model is trained to predict the real age associated with the patient's brain image data (Figure 4.1b).

3: Encoded representations are the output of the encoder.

After employing the chosen method to pre-train the model, the next phase involves transferring the trained model on a specific downstream task, using a dataset of a smaller cohort of patients. Rather than initializing the model f_θ with random weights θ_{rand}, it is initialized with the pre-trained weights

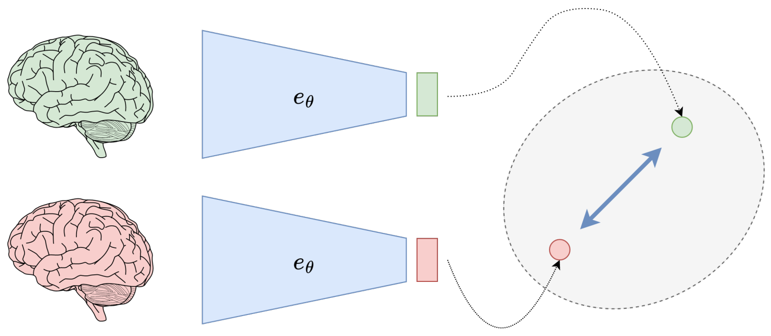

Figure 4.2: The Contrastive Learning method aims at maximizing the distance between the latent representations of the anchor (green) and the latent representations of negative examples (red).

θ_{HC} obtained during the first phase. The fundamental rationale behind this approach is that by allowing the model to first learn the general variabilities present in the data, it will requires significantly less data to subsequently learn the specific features necessary to distinguish between particular conditions. Although all these pre-training methods have proven to be extremely effective, a detailed explanation of them is beyond the scope of this thesis. Given that the current work concentrates on the contrastive learning framework, it is therefore appropriate to shift the discussion on this method.

4.1.2 Supervised Contrastive Learning

As previously mentioned, the foundational principle of the Contrastive Learning [3–8] framework is to develop representations that draw similar items (positive pairs) nearer in the embedding space, while distancing dissimilar items (negative pairs). The model accomplishes this by optimizing a loss function that fosters this specific behavior. Various loss functions [41, 42] have been devised to foster such behavior, but this discussion will specifically focus on those used in the supervised context [4]. To establish a more formal foundation for this discussion, consider a neural network model denoted by f_θ. For any given image and its associated class label (x_i, y_i) from the dataset, one can compute the latent representation[4] $z_i = f_\theta(x_i)$. Let also be $I = \{0, \dots, r\}$ the set of indices in the minibatch, $A(i) = I/i$ the set of indices of all other samples in the minibatch (except the anchor), and $P(i) = \{p \in A(i) \ : \ y_p = y_i\}$ the set of indices of positive samples[5].

[4]: Chen et al. (2020), *A Simple Framework for Contrastive Learning of Visual Representations*

4: Also referred to as the *anchor* in this context.

5: Positive in the sense that they share the same class as the anchor.

In the supervised contrastive learning process, each element of the minibatch $x_i \in \mathcal{B}_r$ is iteratively considered as the anchor. At each step, each positive sample x_p with $p \in P(i)$ is paired with the anchor to form a positive pair. Concurrently, the anchor x_i is paired with each remaining sample x_a with $a \in A(i)$ of the minibatch to form negative pairs. The objective of the loss is to maximize the similarity[6] $s_p = sim(z_i, z_p)$ between embeddings of positive pairs, while minimizing the similarity $s_a = sim(z_i, z_a)$ between negative pairs. The similarity is usually computed though a *Cosine Similarity*, but can be computed with any similarity measure. For any anchor i, this training objective can be computed using the Supervised Contrastive (*SupCon*) Loss function, shown in Equation 4.1.

6: Maximizing the similarity is equivalent to minimizing the distance.

$$\mathcal{L}^{\text{sup}} = -\frac{1}{|P(i)|} \sum_{p \in P(i)} \log \left(\frac{\exp(s_p/\tau)}{\sum\limits_{a \in A(i)} \exp(s_a/\tau)} \right) \tag{4.1}$$

Where the term $\tau \in \mathbb{R}^+$ is a scalar value that indicates the *temperature*[7] of the method. The loss of the entire minibatch is simply the sum of the loss values, considering each element of the minibatch as the anchor.

7: The temperature is an hyperparameter of the loss function that allows to tune the sensitivity of the loss function to differences between the distances of positive and negative pairs in the embedding space.

Models pre-trained with the SupCon loss has shown state of the art accuracy in classification tasks performed on common labelled imaging datasets [4]. One of its obvious limitation is that it needs a large labelled dataset to be applied successfully, which, as discussed previously, is not the common case of neuroimaging datasets.

4.1.3 Self-Supervised Contrastive Learning

In reality, the SupCon loss is a specific case of a more general function designed to work in an unsupervised setting. Instead of relying on labels to the determine the real class of a sample, this method assumes that each sample belongs to its own unique class. By following this principle, the method applies an augmentation[8] $Aug(\cdot)$ to the anchor, obtaining another sample $x_j = Aug(x_i)$ that is treated as positive.

8: A series of transformations including cropping, rotation, and color adjustments, intended to generate a different positive sample that semantically similar to the original sample but vary in some features

The next step is equivalent to the SupCon loss. A positive pair is formed by means of augmentation to the anchor, and negative pairs are formed using all the remaining samples in the minibatch. Equation 4.2 summarizes the Self Supervised

Contrastive loss function.

$$\mathcal{L}^{\text{self}} = -\log\left(\frac{\exp(s_j/\tau)}{\sum_{a\in A(i)} \exp(s_a/\tau)}\right) \tag{4.2}$$

Technically speaking, minimizing these loss formulations corresponds to maximizing the mutual information [43] between positive pair representations, effectively increasing the amount of shared information between a positive representation (z_i) and its augmented sample (z_j). Equation 4.2 can also be interpreted from a probabilistic perspective. Through this lens, the numerator can be seen as assigning a high probability to the event where the anchor and its positive pair are close together in the embedding space. The denominator acts as a normalization factor, summing the exponential similarity scores of the anchor with all other embeddings in the batch (except for itself). This sum transforms the raw exponential scores into probabilities via the softmax function, thus creating a probability distribution[9] over all pairs involving the anchor and a negative sample, where pairs with higher similarity scores are assigned higher probabilities. In essence, the ratio calculates the probability that the anchor z_i is similar to the positive embedding z_j, relative to the probability of being similar to any other negative embedding z_a.

9: Also referred to as the *noise* distribution, as it should include negative samples.

The role of the numerator is to create a "pulling" force between the anchor and its positive counterpart in the embedding space, ensuring that these connections are reinforced more strongly during the training process than any other connections. Conversely, the denominator serves to "push" negative samples away from the anchor in the embedding space.

However, viewing these loss functions from a probabilistic angle also highlights a potential issue. These losses assume that all other samples in the minibatch, aside from the anchor, are negative samples, even though there may be semantically similar samples to the anchor present in the minibatch. In other words, other potentially positive samples could be inadvertently included in the noise distribution.

4.1.4 Weakly-Supervised Contrastive Learning

To address the issue of false negatives in the noise distribution, several studies have proposed modifications to the aforementioned loss functions. These adjustments are classified under the umbrella of weakly supervised strategies. The essence of these strategies is to utilize additional metadata associated with a sample to define closeness in the embedding space. The underlying intuition is that samples from similar classes would also share similar characteristics and, consequently, similar metadata. Augmenting the loss functions with additional information helps refine the distinction between positive and negative pairs, improving the effectiveness of the model in recognizing and differentiating between closely related samples.

[44]: Dufumier et al. (2021), *Contrastive learning with continuous proxy meta-data for 3D MRI classification*

10: This term is used because the model utilizes the target variable y during the pre-training phase.

11: Which could either be a Gaussian or RBF kernel.

In the neuroimaging domain, Dufumier et al. [44] proposed a method that incorporates the age of a patient associated with a brain scan as additional metadata. In their research, a contrastive loss function named *y-aware*[10] was developed. The fundamental concept of this function is to calculate a weight term $0 \leq w_k \leq 1$ that determines the *degree of positiveness* of the k^{th} sample relative to the anchor. To compute this term, the authors suggest applying a kernel[11] K_σ to the age difference between the patients associated with the brain images. Formally, if y_k is the age attribute associated with the k^{th} sample, then the weight term is calculated as shown in Equation 4.3.

$$w_k = K_\sigma(y_i - y_k) \tag{4.3}$$

The role of the kernel K_σ in this context is to constrain the difference value between 0 and 1. The hyper-parameter σ determines the spread of the kernel and can be readily estimated from the dataset.

12: Indeed, the original formulation in Equation 4.1 is a special case of the *y-aware* function, where weights are implicitly set to either 1 or 0, depending on whether x_k belongs to the same class as x_i or not.

The weight term w_k is subsequently incorporated into the SupCon loss formulation by multiplying each pair by its corresponding weight value[12]. This modification allows the model to adjust the influence of each sample pair in the loss calculation based on their relative age difference. Equation 4.4 shows the formulation of the *y-aware loss*.

$$\mathcal{L}^{\text{y-aware}} = -\sum_{k \in A(i)} \frac{w_k}{\sum_t w_t} log\left(\frac{\exp(s_k/\tau)}{\sum\limits_{a \in A(i)} \exp(s_a/\tau)}\right) \tag{4.4}$$

Pre-trained models that employ the *y-aware* loss have subsequently achieved state-of-the-art performance in downstream tasks involving the prediction of neurological pathologies such as Schizophrenia (SCZ), Bipolar Disorder (BD), and Alzheimer's Disease (AD).

Subsequent research has further explored refinements of the *y-aware* loss concept. Specifically, Barbano et al. [45] proposes two extensions to the original formulation. The first refinement arises from the observation that the uniformity term (the denominator) in Equation 4.4 tends to focus more on the closest samples within the representation space. This concentration means that if positive samples exist elsewhere in the minibatch, they are inadvertently included in the noise distribution, thus receiving disproportionately high weighting compared to other negative samples. To address this issue, the uniformity term is adjusted to include only those samples that are more distant from the anchor than the considered x_k in the kernel space. This refinement helps ensure that the term focuses on truly negative samples, thereby reducing the influence of inadvertently included positive samples in the noise distribution. Equation 4.5 shows the proposed loss function that encodes this behaviour.

[45]: Barbano et al. (2023), *Contrastive learning for regression in multi-site brain age prediction*

$$\mathcal{L}^{\text{thr}} = -\sum_{k \in A(i)} \frac{w_k}{\sum_t \delta_{w_t < w_k} w_t} \log \left(\frac{\exp(s_k/\tau)}{\sum_{a \in A(i)} \delta_{w_t < w_k} \exp(s_a/\tau)} \right) \tag{4.5}$$

Where δ_c is a step function whose value are 1 when the condition c is true or 0 otherwise.

The other loss function proposed takes an opposite approach. Rather than repelling the closest "least positive" sample, it adjusts the repulsion strength (i.e., the weight) on the noise distribution in proportion to their distance from the anchor in the kernel space. This method ensures that samples farther away from the anchor exert a greater influence on the noise distribution, thereby refining how the model discriminates between truly negative and potentially positive samples within the embedding.

$$\mathcal{L}^{\text{exp}} = -\sum_{k \in A(i)} \frac{w_k}{\sum_t w_t} \log \left(\frac{\exp(s_k/\tau)}{\sum_{a \in A(i)} \exp((1 - w_t) s_a/\tau)} \right) \tag{4.6}$$

In Equation 4.6, which encapsulates this concept, the weighting factor $(1 - w_t)$ serves as a negative weighting factor, assigning more weight to samples that are farther from the anchor in the kernel space. This adjustment emphasizes the influence of distant samples in the kernel space, effectively pushing them away from the anchor in the embedding space.

To evaluate these loss functions, a 3D CNN was trained specifically to minimize the loss function under consideration. After the training of the CNN, a linear classifier was then trained on the latent representations produced by the CNN, using a smaller validation dataset. Essentially, the CNN model functions to map brain images into a more compact representation space, from which a linear classifier is subsequently trained. In the experiments conducted, the downstream task for which the linear classifier was trained is brain-age prediction. This approach allows to assess the effectiveness of the latent space learned by the CNN and to determine how well the extracted features contribute to estimating brain age. The experiments conducted demonstrated that the loss function $\mathscr{L}^{exp}$ yielded superior results, suggesting that $\mathscr{L}^{exp}$ effectively facilitates the extraction and encoding of relevant features, that improves the model's predictive capabilities on the brain-age prediction task.

All of these weakly supervised loss functions have shown promising experimental results; however, a notable limitation of this class of approaches is their reliance on a single attribute, such as age, to determine the alignment strength (w_k). Consequently, they are not well-suited to leveraging multiple attributes, such as anatomical measurements of the brain. The method proposed in the subsequent section addresses this limitation by extending the weakly contrastive formulation to include multiple attributes, thereby enhancing the model's capacity to capture and utilize a broader spectrum of relevant information.

4.2 AnatCL

To extend the discussed loss functions to include multiple attributes, one of the initial approaches undertaken involved directly modifying the weight computation. A straightforward and quick method to consider is to define the weight as the average of the kernelized differences between each selected attribute. More formally, if the target attribute y is not just a single scalar but a vector $\mathbf{y}$ consisting of L attributes, the resulting weight w_k could be calculated using Equation 4.7.

$$w_k = \frac{1}{L} \sum_{l=0}^{L} K_l(\mathbf{y}_{i,l} - \mathbf{y}_{k,l}) \tag{4.7}$$

This formulation applies the kernel K_l to the difference between each attribute l to derive an attribute-wise similarity value. Subsequently, the mean of these similarity values is calculated to produce a single scalar value. The mean operation is done to ensures that each attribute contributes equally to the overall weight, allowing for a balanced integration of multiple characteristics. Also, in order to accommodate the unique variabilities associated with each attribute, a different kernel K_l is applied to each difference. This initial formulation was first tested using a set of selected attributes—namely age, CerebroSpinal Fluid Volume (CSFV), Gray Matter Volume (GMV), and White Matter Volume (WMV)—made available by the OpenBHB dataset [46]. To evaluate the effectiveness of this new formulation, a 3D ResNet-18 model was pre-trained using this contrastive loss formulation on the OpenBHB dataset. Subsequently, the model was tested on the brain-age prediction task using a test split of the dataset. Although this first approach incorporates more information into the learning process, it demonstrated a decline in performance compared to counterparts that utilize only the single age attribute[13]. The hypothesis is that these anatomical attributes are global features of the brain that may act as confounders for the model [47].

[46]: Dufumier et al. (2022), *OpenBHB: a Large-Scale Multi-Site Brain MRI Data-set for Age Prediction and Debiasing*

13: More precisely, in the downstream task of brain age prediction, the mean squared error (MSE) recorded was 7.29, in contrast to a significantly lower MSE of 2.66 achieved with the baseline method.

[47]: Komeyer et al. (2024), *A framework for confounder considerations in AI-driven precision medicine*

The suboptimal performances observed with this formulation highlighted the need for a different approach to address this problem. Attention shifted specifically to another set of anatomical features derived from the Desikan et al. brain parcellation [25]. As previously discussed in Chapter 3, the Desikan brain parcellation is represented by a matrix $\mathcal{D} \in \mathbb{R}^{68\times7}$, where each row contains a vector of 7 features. Each vector represents a set of anatomical features measured in a specific brain area. Despite offering a richer and more nuanced representation of anatomical features, the Desikan parcellation presents challenges due to the multi-dimensional nature of its data. This complexity poses difficulties in formulating an effective similarity measure, as the previously discussed loss

[25]: Desikan et al. (2006), *An automated labeling system for subdividing the human cerebral cortex on MRI scans into gyral based regions of interest*

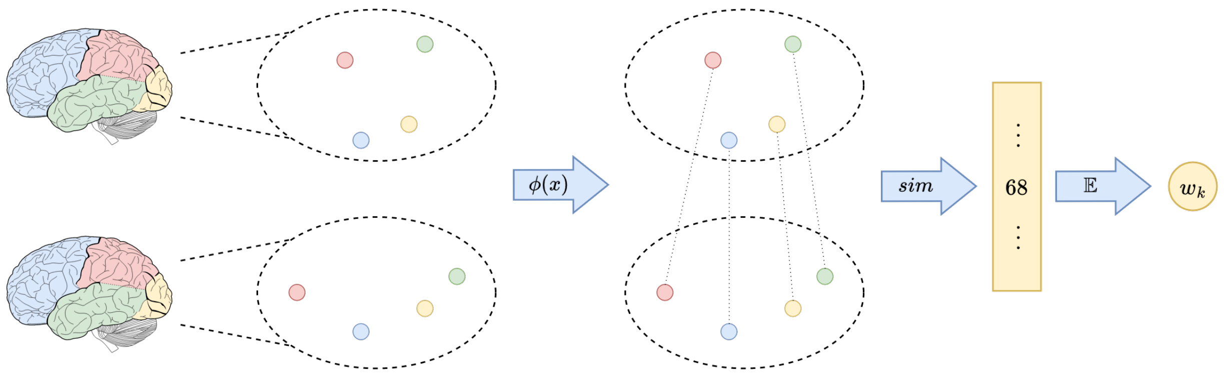

Figure 4.3: Graphical depiction of the steps required to compute the local descriptor. In this interpretation, two different Desikan parcellations are visualized as a series of 68 points within a 7-dimensional space. The first step in computing the local descriptor involves normalizing these vectors through the function $\gamma(x)$, ensuring that they are positioned on the unit hypersphere. Following normalization, the next step involves calculating the pairwise similarities between each measurement vector, resulting in a vector of 68 similarity values. Each value reflects the closeness between corresponding brain regions in terms of their anatomical features. To determine the final degree of positiveness, which quantifies the overall similarity between the two parcellations, the expected value $\mathbb{E}$ is computed across the similarity vector.

formulations have primarily addressed scalar feature values. To incorporate these measurements effectively, it is essential to define a robust similarity measure between two Desikan parcellations.

4.2.1 Local Descriptor

Two different formulations were hypothesized based on the interpretation of the Desikan parcellation. The first arises from viewing the Desikan parcellation as comprised of 68 vectors of 7 anatomical measurements. According to this interpretation, the proposed method to compare two parcellations involves calculating the pairwise similarity between each corresponding measurement, resulting in a vector of 68 similarity values. Each value in this vector indicates the degree of closeness between the corresponding brain regions in terms of the recorded anatomical features. Finally, the expected similarity value across all measurements is then used as the degree of positiveness that can be subsequently used in one of the weakly contrastive loss formulations discussed earlier. Since with this interpretation the degree of positiveness is obtained by computing the expected value of the cross-region similarities, it has been called *"local descriptor"*. Formally, the Desikan parcellation of a i^{th} sample is represented as $\mathcal{D}^i \in \mathbb{R}^{68\times7}$. Each row $\mathcal{D}^i_n$ denotes the measurement vector for the n^{th} brain region of the i^{th} patient. Before proceeding with cross-similarity calculations, an adjustment must be made due to the fact that each feature within a measurement vector captures specific anatomical information and is recorded on a scale that differs from other measurements within the vector. To address this variability, a normalization[14] $\gamma(x)$ is applied to each vector to standardize all measurements. Following this approach, Equation 4.8 illustrates the formulation of the discussed local descriptor.

14: A transformation used to rescale values to a range of $[0;1]$. An example of a normalization is the min-max normalization.

$$w_k = \frac{1}{68} \sum_{n=1}^{68} sim(\gamma(\mathcal{D}_n^i), \gamma(\mathcal{D}_n^k)) \tag{4.8}$$

Where $sim(x, y)$ can be any similarity function[15]. In this case, the w_k term calculates the atlas-wise similarity of the k^{th} parcellation in relation to the anchor parcellation i.

15: In this work the Cosine Similarity has been mainly used.

4.2.2 Global Descriptor

The global descriptor derives from interpreting the Desikan format from another point of view. Rather than viewing the data as 68 measurement vectors, each containing 7 different features, this approach considers the format as 7 feature vectors, each composed of 68 measurement values. Each vector encompasses the values of a specific measurement recorded across all 68 brain areas. This reorganization shifts the focus from the regional to the feature-specific analysis, facilitating a global evaluation that highlights how each individual anatomical characteristic varies across different brain regions. In other words, this interpretation arises from considering the transposed version of the Desikan parcellation, denoted as $\mathcal{D}^T$, which transforms the matrix into a 7×68 dimensional format. This transposition shifts the focus from regional measurements to a feature-centric analysis, allowing each row of the matrix to represent all the measurements of a specific feature across the 68 brain regions. Since each row of the transposed $\mathcal{D}^T$ matrix contains measurements of a specific feature across different regions, all data are maintained on a consistent scale. This uniformity across each vector means that no normalization step is required before computing the similarity values, simplifying the process and ensuring that the original measurement scales are preserved during analysis. Equation 4.9 shows the formulation of the global descriptor, where $\omega_n^i = \left(\mathcal{D}^i\right)_n^T$ is the row vector of the transposed parcellation of the i^{th} sample, containing the 68

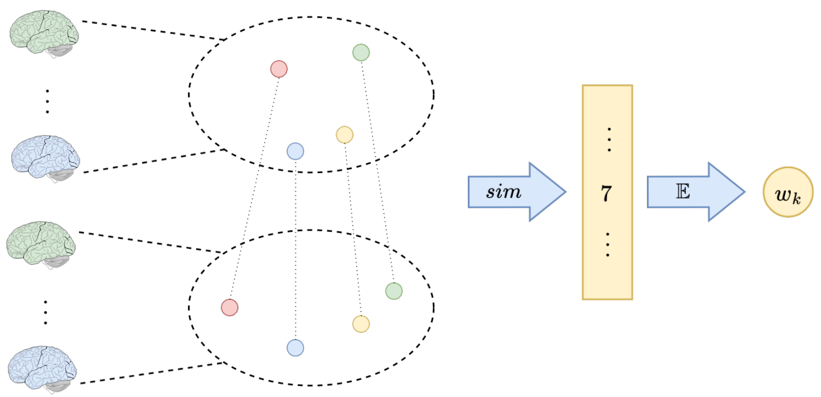

Figure 4.4: In the corresponding visualization, each brain, colored distinctively, represents a specific feature vector, which can be depicted in a 68-dimensional space. The global descriptor involves computing the cross-similarity, resulting in a 7-element vector that contains feature-wise similarities. Similar to the local descriptor, the expected value of this vector is calculated to determine the degree of positiveness.

measurements pertaining the n^{th} feature.

$$w_k = \frac{1}{7}\sum_{n=1}^{7} sim(\omega_n^i, \omega_n^k) \tag{4.9}$$

Both the local and global descriptor can then be utilized to calculate the w_k term in one of the weakly supervised contrastive loss formulations previously discussed. Given that this loss relies on anatomical measures, it has been designated as $\mathcal{L}^{\text{AnatCL}}$.

To incorporate also the age attribute into the final objective loss, the resulting function is structured as a weighted sum. This sum combines a weakly supervised loss that is augmented with the age attribute ($\mathcal{L}^{\text{age}}$) and another weakly supervised loss that utilizes the anatomical information ($\mathcal{L}^{\text{AnatCL}}$). The specific formulation of this final objective loss is detailed in Equation 4.10.

$$\mathcal{L} = \lambda_1 \mathcal{L}^{\text{age}} + \lambda_2 \mathcal{L}^{\text{AnatCL}} \tag{4.10}$$

In the formulation of the final objective loss function, $\mathcal{L}^{\text{age}}$ represents any of the previously discussed weakly supervised loss functions where the computation of the degree of positiveness is determined using the age attribute. Conversely, $\mathcal{L}^{\text{AnatCL}}$ refers to a weakly supervised loss where the degree of positiveness is computed using either the local or global descriptor, depending on the specific anatomical features considered. Additionally, $\lambda_1, \lambda_2 \in \mathbb{R}$ serve as scalar hyperparameters within the loss function. These parameters are used to weigh the importance of each loss component, thereby determining the preference between $\mathcal{L}^{\text{age}}$ and $\mathcal{L}^{\text{AnatCL}}$. Adjusting these values allows for fine-tuning of the model's

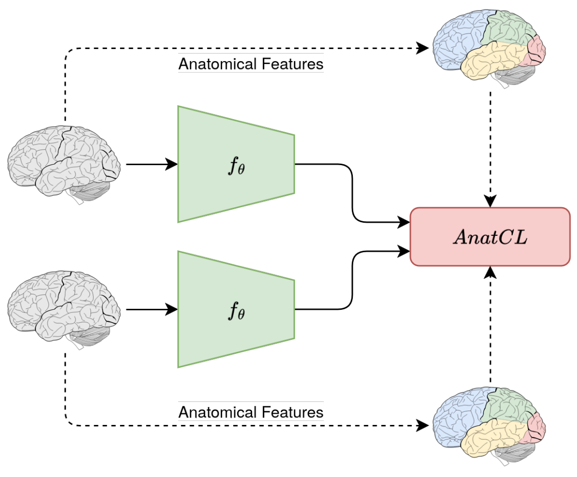

Figure 4.5: AnatCL loss overview.

sensitivity to either the chronological age or the anatomical features, optimizing the balance based on specific predictive goals or dataset characteristics.

Experiments 5

This chapter outlines the experiments conducted to assess the efficacy of the proposed loss formulation. To facilitate a comprehensive evaluation, multiple neuroimaging datasets were utilized, which are described in a dedicated section. Subsequent to dataset descriptions, the experimental setup is thoroughly detailed, including the model used and all pertinent training parameters. Finally, the chapter concludes with several sections, each dedicated to discussing the experimental results for a specific task that was tested.

5.1 Datasets

Overall, the experimental data consisted of T1-weighted MRI scans, totaling 21,155 images from 7,908 individuals. This data was sourced from various publicly available datasets, encompassing five different neurological conditions. The conditions and respective datasets include healthy samples from OpenBHB [46], Alzheimer's Disease from ADNI [48] and OASIS-3 [49], schizophrenia from SchizConnect [50], and Autism Spectrum Disorder from ABIDE I [51]. This diverse compilation of datasets provided a robust foundation for evaluating the proposed loss formulation and its effectiveness across different neurological conditions. The overall composition of the cohorts used in this study is presented in Table 5.1.

Condition	Dataset	Patients
Healthy Control	OpenBHB	3984
Schizophrenia	SchizConnect	383
Alzheimer's Disease	ADNI	1754
Alzheimer's Disease	OASIS-3	685
Autism Spectrum Disorder	ABIDE-I	1102

Table 5.1: An overview of the various datasets utilized in this study, along with their cohort compositions.

5.1.1 OpenBHB

OpenBHB is a newly released dataset that consolidates healthy control (HC) samples from numerous public cohorts including ABIDE 1, ABIDE 2, CoRR, GSP, IXI, Localizer, MPI-Leipzig, NAR, NPC, and RBP. Each scan in this dataset originates from a different subject, making it uniquely suited for ensuring diversity in the training process. In addition to structural scans and patient information[1], OpenBHB provides seven anatomical measures based on the Desikan-Killiany parcellation [25]. As previously discussed, such measures include cortical thickness (mean and standard deviation), gray matter volume, surface area, integrated mean, Gaussian curvature index, and intrinsic curvature index [46].

1: Some of them are age, sex, total intracranial volume, acquisition settings.

5.1.2 ADNI

The Alzheimer's Disease Neuroimaging Initiative (ADNI) is a significant research project that was launched to study Alzheimer's disease through the collection and analysis of medical imaging, genetic, biological markers, and clinical assessment data. ADNI is aimed at understanding the progression of Alzheimer's Disease from its earliest stages, through mild cognitive impairment (MCI), to full Alzheimer's Dementia (AD). Over the years, several phases of the Alzheimer's Disease Neuroimaging Initiative (ADNI) have been undertaken, each contributing to the growing body of data on Alzheimer's Disease and its precursors. The specific phases include ADNI-1, ADNI-2, ADNI-GO, and ADNI-3. For the experiments conducted, data from all these different ADNI phases were utilized, comprising a diverse cohort of participants. This included 633 healthy controls (HC), 712 patients diagnosed with mild cognitive impairment (MCI), and 409 patients diagnosed with Alzheimer's Disease (AD).

5.1.3 OASIS-3

The Open Access Series of Imaging Studies (OASIS-3) is a neuroimaging dataset specifically designed for studying the progression of Alzheimer's disease across different stages. OASIS-3 builds upon earlier versions of the dataset (OASIS-1 and OASIS-2) by incorporating a larger and more diverse set of data points, which includes both longitudinal and cross-sectional data. The dataset contains a demographic of participants ranging from young adults to older adults with varying stages of cognitive decline, including normal aging individuals, those with Mild Cognitive Impairment (MCI), and those diagnosed with Alzheimer's disease. For the experiments conducted with this dataset, 685 patients were included, containing 88 AD cases.

5.1.4 SchizConnect

SchizConnect is a dataset that emerged from a collaborative research effort aimed at consolidating neuroimaging data from multiple studies and sites. It includes participants diagnosed with schizophrenia, schizoaffective disorder, other related psychotic disorders, and healthy control individuals. From the SchizConnect database, anatomical MRIs were included for the experiments, for a total of 383 patients. This cohort is categorized as follows: 180 are healthy controls (HC), 102 are classified under schizophrenia (broad), 74 under schizophrenia (strict), 11 as schizoaffective patients, and 9 with bipolar disorder.

5.1.5 ABIDE I

The Autism Brain Imaging Data Exchange I (ABIDE-I) is an open-source initiative designed to support research into Autism Spectrum Disorder (ASD). ABIDE-I encompasses a comprehensive dataset comprising resting-state functional magnetic resonance imaging (rs-fMRI) scans, anatomical scans, and phenotypic information from over 1,000 individuals, ranging in age from 6 to 64 years. This diverse group includes both individuals diagnosed with ASD and age-matched control subjects without ASD, providing a robust resource for comparative studies.

In the conducted experiments, anatomical MRIs from ABIDE-I were utilized, involving a total of 1,102 participants. This cohort was categorized into 556 healthy controls (HC), 339 patients diagnosed with autism, 93 patients with Asperger's Syndrome, and 7 diagnosed with pervasive developmental disorder not otherwise specified (PDD-NOS).

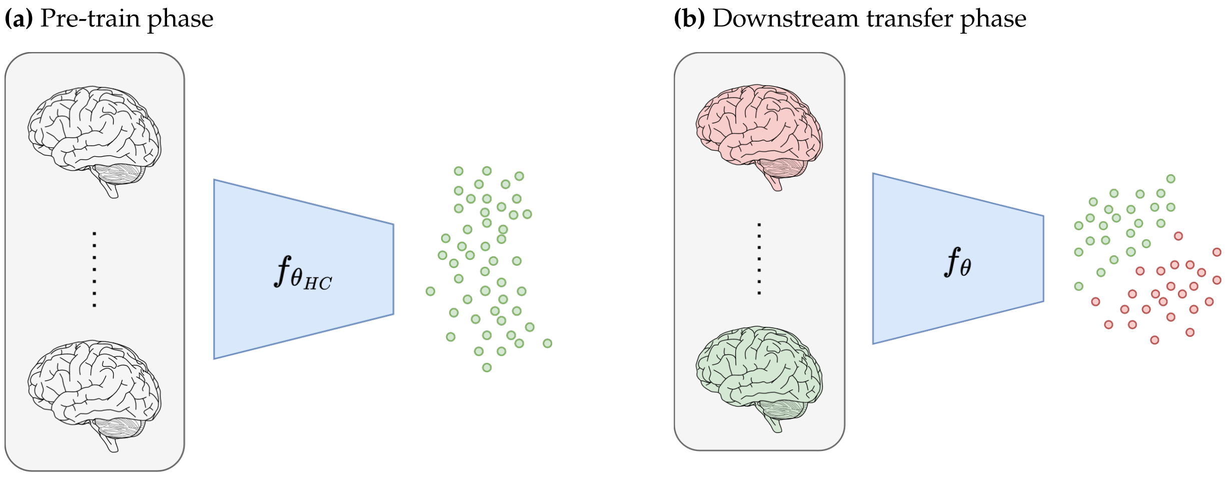

Figure 5.1: The experimental settings adhere to the principles of transfer learning. Initially, a model f (depicted in blue) is pre-trained on a substantial cohort of healthy subjects (represented by the grey box), utilizing the OpenBHB dataset in this instance. The outcome of this initial phase is a model $f_{\theta_{HC}}$, which has captured general variabilities within the data; that is, it has learned the latent *manifold*. In the subsequent phase, the model is adapted to a downstream task. This involves mapping the images into the learned latent space, after which a conventional machine learning model is employed to perform the classification.

5.2 Experimental Settings

Before initiating any experiments, to ensure uniformity across all images, they underwent a standardized VBM preprocessing protocol using CAT12 [32]. This preprocessing included non-linear registration to the MNI template and extraction of gray matter (GM). The images were brought to a final spatial resolution of 1.5mm isotropic and sized to 121 x 145 x 121. The preprocessing tasks were carried out using the BrainPrep package [31]. The experiments specifically utilized modulated gray matter (GM) images, as indicated by Dufumier et al. [46], to ensure that the volumetric information was retained in the images for detailed analysis.

[31]: Grigis et al. (2022), *BrainPrep*

The experiments followed a two-phased approach aligned with the transfer learning paradigm. Initially, a target model was pre-trained using the proposed contrastive learning loss on the OpenBHB dataset. Subsequently, the model was tested on various downstream tasks across different datasets to assess its performance and generalization capabilities. Practically, in the proposed losses (Eq. 4.7, Eq. 4.8), only a subset of the anatomical measurements available in the Desikan format were utilized[2]. These losses are henceforth referred to as AnatCL-G3 for the global descriptor version using three measurements and AnatCL-L3 for the corresponding local descriptor.

2: Specifically Cortical Thickness (CT), Gray Matter Volume (GMV), and Surface Area (SA).

The experimental settings for both loss formulations, local (AnatCL-L3) and global (AnatCL-G3), were identical. Two ResNet-18 3D models were pre-trained using VBM-preprocessed images along with their corresponding Desikan measures based on the proposed formulations. The training process utilized the Adam optimizer with a learning rate of 0.0001 and a decay rate of 0.9 applied every 10 epochs. The models were trained with a batch size of 32 for a total of 300 epochs. For simplicity, the values of λ_1 and λ_2 were both set to 1. As is standard practice in contrastive learning approaches [4, 5], the contrastive loss was computed using a fully-connected projection head following the encoder, which consisted of two layers.

To endure a robust evaluation, the experimental setup included cross-validation, where each of the 5 folds was structured with a 70% training split and a 30% test split. This distribution ensured that each fold had a substantial amount of data for training the models, while still providing a significant portion for testing and evaluating model performance across different iterations. The results were then quantified in terms of mean and standard deviation across the 5 folds, providing a comprehensive assessment of model performance and stability across different test scenarios.

After the pre-training step, the models underwent evaluation by testing their performance using a transfer learning approach. In this approach, latent representations were first generated by the model using only the encoder section, discarding the fully connected head[3]. For each downstream task, a different linear classifier was trained on these extracted representations to assess the model's ability to learn meaningful and generalizable features. The rationale behind this methodology was to isolate the effectiveness of the learned representations from the specific architecture of the downstream task classifiers. By focusing on the encoder's output, the evaluation could better determine whether the fundamental features extracted during pre-training were robust and informative enough to facilitate accurate classifications across various conditions, independent of the subsequent classifier configurations.

3: This step ensures that the evaluation focuses on the quality of the features extracted by the encoder, rather than the classification capabilities of the full network.

The downstream tasks primarily focused on predicting specific diagnoses (such as Alzheimer's Disease, Schizophrenia, Bipolar Disorder, etc.), biomarkers (e.g., brain age), or phenotypes (e.g., sex). Additionally, other relevant clinical assessments included in the datasets were also considered, which will be explained in detail in Section 5.4. A total of 22 downstream tasks were tested, which are summarized in Table 5.2. For the comparative analysis with standard approaches, four different baseline methodologies were also tested alongside the proposed method. These included the completely self-supervised loss, known as SimCLR [4] (Eq. 4.2), and three supervised baselines: a standard model trained with the L1 loss [5], y-Aware (Eq. 4.4), and ExpW (Eq. 4.6). To ensure consistency and fairness in the evaluation, all these methods were subjected to the same experimental setup as previously described. In this way, the comparative results accurately reflect the relative performance of each method under identical conditions. All the experiments were implemented in PyTorch [15] and run on a cluster of 4 NVIDIA V100 GPUs[6], with each training session taking approximately 10 hours.

Table 5.2: Summary of downstream tasks (12) and clinical assessment scores (10) considered in the study.

Dataset	Task / Condition	Dataset	Phenotype
OpenBHB	Age (HC)	SchizConnect	AIMS Overall Severity
	Sex		AIMS Upper Body
ADNI	Alzheimer's Disease		AIMS Lower Body
	sMCI vs pMCI		Depression
OASIS-3	Alzheimer's Disease		Handedness
SchizConnect	Schizophrenia Broad		SAS GAIT
	Schizophrenia Strict	ABIDE 1	Handedness
	Bipolar Disorder		FIQ (WASI)
	Schizoaffective		VIQ (WASI)
ABIDE I	Autism		PIQ (WASI)
	Aspergers		
	PDD-NOS		

4: This loss was introduced by the authors of the corresponding paper [4] and is referenced as such.

5: An L1 loss function calculates the mean of the absolute differences between the labels and the predictions.

6: The computational resources were provided by the Leonardo supercomputer, which is managed by the CINECA consortium.

5.3 Diagnosis Prediction

5.3.1 Brain Age and Sex Prediction

Preliminary results focusing on brain age prediction and sex classification were evaluated using the OpenBHB dataset. These results are detailed in Table 5.3. Analysis of the findings indicates that the AnatCL model is capable of matching and slightly exceeding state-of-the-art performance in brain

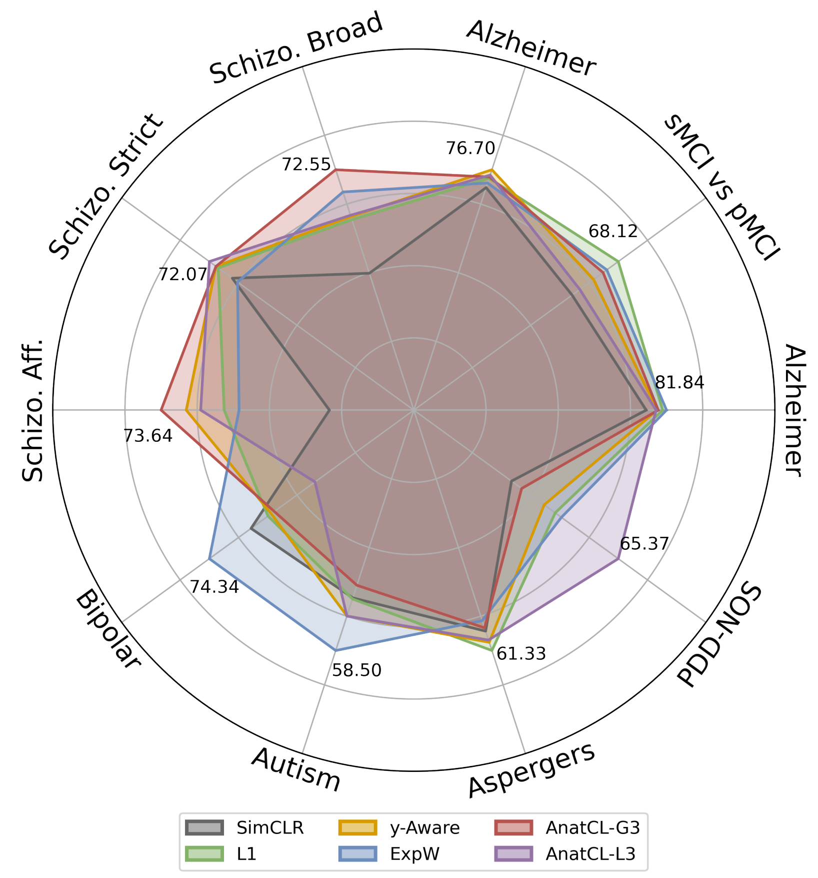

Figure 5.2: A polar plot that summarize the performances of the various loss functions discussed in this chapter.

age prediction tasks. It is important to note that no bias-correction methods were employed in this study, despite recommendations suggested by Cumplido-Mayoral et al. [52] and Lange and Cole [53]. In terms of sex classification, while the AnatCL model does not outperform the ExpW approach, it does show improvements over the SimCLR and L1 loss baselines.

Method	Age MAE	Sex
SimCLR	$5.58_{\pm 0.53}$	$76.7_{\pm 1.67}$
L1 (age sup.)	$2.73_{\pm 0.14}$	$76.7_{\pm 0.67}$
y-Aware	$2.66_{\pm 0.06}$	$79.6_{\pm 1.13}$
ExpW	$2.70_{\pm 0.06}$	$\mathbf{80.3}_{\pm 1.7}$
AnatCL-G3	$\mathbf{2.61}_{\pm 0.08}$	$78.2_{\pm 1.25}$
AnatCL-L3	$2.64_{\pm 0.07}$	$78.2_{\pm 0.7}$

Table 5.3: Results on OpenBHB in terms of mean absolute error (MAE) on age prediction, and balanced accuracy on sex classification.

5.3.2 Alzheimer's disease and Cognitive Impariments

In Table 5.4, the results for Alzheimer's Disease (AD) detection using the ADNI and OASIS-3 datasets are presented. Although the AnatCL model does not achieve the best results overall, it generally shows improvements over the self-supervised baseline (SimCLR) and occasionally surpasses the performance of either the L1, y-Aware, or ExpW models. This indicates that while AnatCL may not yet be the top-performing model across all metrics, it demonstrates potential by consistently outperforming a self-supervised approach and, in some cases, other supervised methodologies. This suggests that further refinement and adaptation of the AnatCL approach could lead to more competitive results in AD detection tasks, as will be discussed in Chapter 6.

Table 5.4: Results on Alzheimer's Disease (AD) classification in terms of balanced accuracy.

	ADNI		OASIS-3
Method	**HC vs AD**	**sMCI vs pMCI**	**HC vs AD**
SimCLR	$78.47_{\pm 2.51}$	$61.77_{\pm 3.85}$	$73.97_{\pm 4.98}$
L1 (age sup.)	$81.20_{\pm 2.3}$	$\mathbf{68.12}_{\pm 5.42}$	$75.40_{\pm 5.4}$
y-Aware	$80.3_{\pm 1.8}$	$64.72_{\pm 4.43}$	$\mathbf{76.70}_{\pm 3.30}$
ExpW	$\mathbf{81.84}_{\pm 2.95}$	$66.54_{\pm 5.64}$	$74.67_{\pm 2.87}$
AnatCL-G3	$80.47_{\pm 2.95}$	$66.03_{\pm 2.93}$	$75.59_{\pm 2.67}$
AnatCL-L3	$80.11_{\pm 1.0}$	$62.83_{\pm 4.5}$	$75.88_{\pm 3.0}$

5.3.3 Schizophrenia and Bipolar Disorders

The performance of downstream tasks on SchizConnect was evaluated for detecting schizophrenia (broad and strict), schizoaffective, and bipolar disorders. The results, detailed in Table 5.5, show that with the AnatCL model, state-of-the-art performance was achieved in three out of the four tasks. This underscores the value of incorporating anatomical information into the model, particularly for these psychiatric conditions.

5.3.4 Autism Spectrum Disorder

Additionally, the performance in detecting Autism Spectrum Disorder (ASD) across three categories—autism, Asperger's,

Table 5.5: Results on schizophrenia detection (SCZ) in terms of balanced accuracy.

	SchizConnect			
Method	**SCZ. (Broad)**	**SCZ (Strict)**	**Schizoaff.**	**Bipolar**
SimCLR	$58.53_{\pm 3.52}$	$68.47_{\pm 8.47}$	$51.23_{\pm 11.94}$	$67.34_{\pm 9.96}$
L1	$65.79_{\pm 4.74}$	$70.68_{\pm 5.10}$	$65.24_{\pm 15.21}$	$64.49_{\pm 22.08}$
y-Aware	$66.20_{\pm 4.50}$	$71.04_{\pm 2.31}$	$70.29_{\pm 14.73}$	$63.95_{\pm 19.81}$
ExpW	$69.53_{\pm 4.43}$	$67.65_{\pm 8.27}$	$63.26_{\pm 18.06}$	$\mathbf{74.34}_{\pm 18.95}$
AnatCL-G3	$\mathbf{72.55}_{\pm 5.16}$	$71.03_{\pm 8.53}$	$\mathbf{73.65}_{\pm 7.29}$	$63.43_{\pm 15.94}$
AnatCL-L3	$66.38_{\pm 5.96}$	$\mathbf{72.07}_{\pm 8.42}$	$68.37_{\pm 8.60}$	$56.60_{\pm 11.48}$

and PDD-NOS—is also reported in Table 5.6. While AnatCL did not outperform other methods for autism and Asperger's patients, it significantly improved accuracy for diagnosing patients with PDD-NOS, a relatively rarer diagnosis within the dataset.

	ABIDE-I		
Method	**Autism**	**Aspergers**	**PDD-NOS**
SimCLR	$54.45_{\pm 2.99}$	$59.61_{\pm 2.72}$	$52.12_{\pm 6.62}$
L1	$54.53_{\pm 1.79}$	$\mathbf{61.33}_{\pm 8.77}$	$57.54_{\pm 5.93}$
y-Aware	$55.84_{\pm 3.37}$	$60.60_{\pm 9.22}$	$56.17_{\pm 10.17}$
ExpW	$\mathbf{58.50}_{\pm 2.41}$	$58.68_{\pm 3.82}$	$58.31_{\pm 4.33}$
AnatCL-G3	$53.48_{\pm 0.99}$	$59.32_{\pm 6.58}$	$53.38_{\pm 5.86}$
AnatCL-L3	$55.85_{\pm 1.02}$	$60.40_{\pm 2.29}$	$\mathbf{65.37}_{\pm 6.73}$

Table 5.6: Results on autism spectrum disorder (ASD) detection in terms of balanced accuracy.

Overall, AnatCL consistently outperformed or matched the other baselines, demonstrating its efficacy across a diverse range of psychiatric conditions. This suggests that AnatCL's approach to integrating detailed anatomical features significantly contributes to its ability to detect nuanced differences in neuroimaging data associated with various psychiatric diagnoses.

5.4 Cognitive Scores/Assessments Prediction

In the final experiments, the focus shifts to predicting clinical assessment scores from brain MRIs, a topic that, to the best of current knowledge, has not been extensively explored in other studies. Specifically, for the SchizConnect dataset,

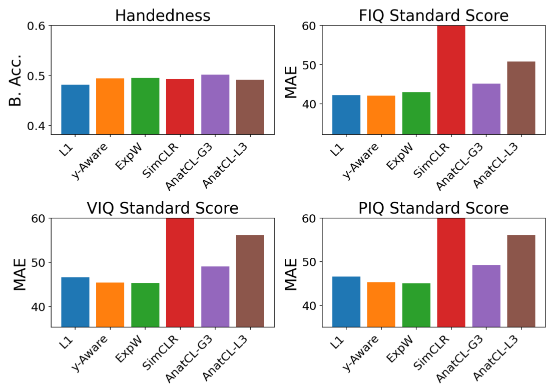

(a)

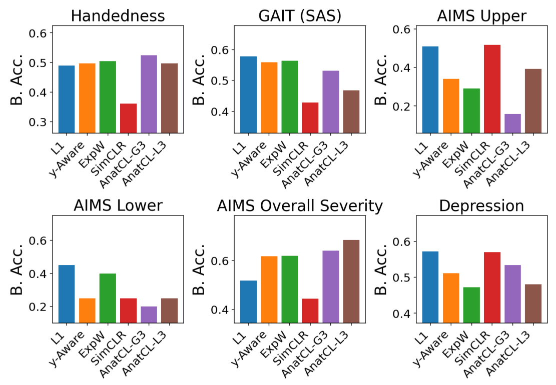

(b)

Figure 5.3: Bar plot format summarization of the results discussed. Subfigure 5.3a refers to the ABIDE-I dataset, while subfigure 5.3b on the SchizConnect.

evaluations included the Abnormal Involuntary Movement Scale (AIMS) assessed across three domains (overall, upper body, lower body), a Depression score based on the Calgary Scale, Handedness information, and GAIT measurements with the Simpson-Angus-Scale (SAS). For the ABIDE dataset, assessments also included handedness and three IQ scores[7]: Full Scale IQ (FIQ), Visual IQ (VIQ), and Performance IQ (PIQ).

7: IQ scores were measured using the Wechsler Abbreviated Scale (WASI)

The ten phenotypes considered are divided based on the nature of the prediction task: AIMS, depression, handedness, and GAIT are approached as classification tasks, while IQ scores (FIQ, VIQ, and PIQ) are treated as regression tasks. More precisely, for handedness, the model predicts right-handed versus other (left-handed or ambidextrous); for depression, it classifies between absent versus mild and above; for AIMS, it differentiates between none and minimal versus mild and above; and for GAIT, it categorizes as normal versus everything else The results of these experiments on the SchizConnect dataset are reported in Table 5.7, while the

Table 5.7: Results of assessment scores/phenotypes prediction from brain MRIs on the SchizConnect dataset.

	SchizConnect					
Method	**AIMS Overall**	**AIMS Up.**	**AIMS Low.**	**Depression**	**Handedness**	**GAIT**
SimCLR	$44.33_{\pm 29.92}$	$\mathbf{51.67}_{\pm 16.16}$	$25.00_{\pm 27.39}$	$56.93_{\pm 13.88}$	$36.06_{\pm 2.72}$	$42.83_{\pm 9.61}$
L1	$51.83_{\pm 24.43}$	$50.83_{\pm 20.82}$	$\mathbf{45.00}_{\pm 33.17}$	$\mathbf{57.17}_{\pm 13.06}$	$48.91_{\pm 5.60}$	$\mathbf{57.73}_{\pm 8.64}$
y-Aware	$61.83_{\pm 15.87}$	$34.17_{\pm 11.90}$	$25.00_{\pm 27.39}$	$51.09_{\pm 5.32}$	$49.71_{\pm 7.69}$	$55.92_{\pm 9.52}$
ExpW	$62.00_{\pm 12.40}$	$29.17_{\pm 17.08}$	$40.00_{\pm 33.91}$	$47.26_{\pm 7.27}$	$50.39_{\pm 6.28}$	$56.39_{\pm 14.14}$
AnatCL-G3	$64.00_{\pm 12.72}$	$15.83_{\pm 12.19}$	$20.00_{\pm 18.71}$	$53.35_{\pm 8.54}$	$\mathbf{52.44}_{\pm 9.14}$	$53.10_{\pm 11.69}$
AnatCL-L3	$\mathbf{68.50}_{\pm 18.09}$	$39.17_{\pm 14.81}$	$25.00_{\pm 27.39}$	$48.05_{\pm 10.89}$	$49.67_{\pm 8.06}$	$46.74_{\pm 5.05}$

results regarding the ABIDE-I dataset are reported in Table 5.8.

Table 5.8: Results of assessment scores/phenotypes prediction from brain MRIs on the ABIDE-I dataset.

	ABIDE-I			
Method	**Handedness**	**FIQ (MAE)**	**VIQ (MAE)**	**PIQ (MAE)**
SimCLR	49.26$_{\pm 5.78}$	84.65$_{\pm 16.36}$	89.07$_{\pm 15.14}$	89.68$_{\pm 15.00}$
L1	48.18$_{\pm 9.43}$	42.16$_{\pm 31.17}$	46.54$_{\pm 32.57}$	46.64$_{\pm 32.24}$
y-Aware	49.45$_{\pm 1.56}$	**42.10**$_{\pm 31.14}$	45.38$_{\pm 33.19}$	45.35$_{\pm 32.76}$
ExpW	49.53$_{\pm 3.26}$	42.94$_{\pm 30.76}$	**45.28**$_{\pm 33.23}$	**45.02**$_{\pm 32.88}$
AnatCL-G3	**50.21**$_{\pm 6.82}$	45.18$_{\pm 29.68}$	49.07$_{\pm 31.52}$	49.30$_{\pm 30.86}$
AnatCL-L3	49.13$_{\pm 3.32}$	50.77$_{\pm 27.14}$	56.18$_{\pm 28.06}$	56.13$_{\pm 27.62}$

While it cannot be concluded that any of the analyzed methods can accurately predict all clinical assessments from MRI scans, AnatCL overall achieves the best results in three out of ten cases, which surpasses any other baseline method. Interestingly, AnatCL shows a better capability to predict the overall AIMS score and patients' handedness. This suggests that there may be a link between brain anatomy and these specific phenotypes, highlighting the potential of anatomically informed models in understanding and predicting behavioral traits.

6 Conclusions and Future Developments

In conclusion, the extensive validation across ten different downstream tasks, as discussed in Chapter 4, has demonstrated that integrating anatomical information during training enhances the accuracy of predictions for various neurological and psychiatric conditions. The findings also indicate a partial improvement in the accuracy for clinical assessment scores and phenotypes. These results suggest that enriching these learning methods with anatomical data can yield more robust and generalizable models applicable to a range of downstream tasks. The insights gained from these models could be crucial in developing personalized treatment plans for patients. By accurately characterizing the neurological basis of various psychiatric and neurodegenerative disorders, these models could significantly influence the design of tailored therapeutic interventions. Additionally, achieving higher accuracy in detecting biomarkers such as brain age from these models could significantly enhance the diagnosis of specific neurological disorders, thereby improving patient outcomes.

However, further research is required to refine and enhance these methods. For example, an obvious limitation of this approach is that these methods still rely on the age attribute, which may not be available in all neuroimaging datasets. Further research in this area could lead to the development of novel methods that rely solely on anatomical measures for weak supervision, potentially achieving superior performance compared to fully self-supervised methods. Since anatomical measures can be automatically extracted using established neuroimaging algorithms, these innovative methods could essentially be considered fully self-supervised.

Furthermore, this research primarily utilized a specific brain atlas, thereby not incorporating the range of other atlases available in the neuroimaging literature. Future work could involve exploring additional atlases that utilize different anatomical measures. Such an endeavor would necessitate a meticulous comparative evaluation of these alternative atlases to determine their efficacy and accuracy relative to the one used in this study. Expanding the scope to include a variety of atlases could enhance the robustness and applicability of the findings, potentially offering a more comprehensive understanding of brain anatomy and its implications for neuroimaging analysis.

Another potential direction not explored in this thesis involves utilizing other acquisition methods as additional learning data. The aim would be to integrate diverse neuroimaging modalities (sMRI, fMRI, dMRI), signals (EEG) and other relevant data (clinical assessment scores, phenotypic data) into the learning process of the model. The idea is to create a more holistic model that incorporates a broader range of modalities in order to provide a more comprehensive understanding of brain health and pathology. The integration of diverse sources of information could be achieved either by incorporating it into the loss formulation, as examined in this work, or by developing a novel multimodal model architecture capable of extracting and combining salient information from input data. Recent research [54] has also demonstrated the feasibility of augmenting deep learning models not only with imaging data but also with textual data. For instance, in the medical domain, there has been a research effort [55] directed towards integrating clinical records and assessment scores. This research direction is further supported by recent works [56] that demonstrated by integrating data of different nature such as EEG and clinical assessments could significantly enrich the representations learned by the model.

[54]: Radford et al. (2021), *Learning Transferable Visual Models From Natural Language Supervision*

[55]: Wang et al. (2022), *MedCLIP: Contrastive Learning from Unpaired Medical Images and Text*

[56]: Venugopalan et al. (2021), *Multimodal deep learning models for early detection of Alzheimer's disease stage*

The findings from this research direction could pave the way for the development of large multimodal models that could serve as foundational tools in personalized medicine. Employing the principles of transfer learning, these models can be adapted for personalized predictions of psychiatric conditions, such as Autism Spectrum Disorder (ASD), and neurodegenerative conditions, such as Alzheimer's Disease (AD). To achieve this, multimodal and/or longitudinal data can be utilized to create detailed, patient-specific profiles and to model the progression of various conditions. Such personalized models can then offer customized insights and treatment recommendations, thereby enhancing patient outcomes by accommodating the unique variations in brain structure and function specific to each individual.

Ethical Considerations

In the development and experiments described within this thesis, strict adherence to ethical standards was maintained. A significant aspect of these ethical considerations involves the use of data. It is important to note that there were no ethical issues concerning the datasets utilized, as all were publicly accessible and composed of previously anonymized patient data, ensuring that individual privacy was preserved and that the data could be used without compromising patient confidentiality.

Furthermore, the applications of the findings discussed in this research thesis are aimed at enhancing the accuracy of diagnoses and the identification of pathological conditions related to the brain. By improving diagnostic capabilities through more precise imaging analysis, the potential for positive impacts on patient outcomes is significant. The use of advanced machine learning models in medical imaging can lead to earlier detection of diseases, more tailored treatment plans, and ultimately, better patient care. This alignment with the goal of improving healthcare outcomes further supports the ethical justification for this research.

Declaration of Originality

I declare to be responsible for the content I'm presenting in order to obtain the final degree, not to have plagiarized in all or part of, the work produced by others and having cited original sources in consistent way with current plagiarism regulations and copyright. I am also aware that in case of false declaration, I could incur in law penalties and my admission to final exam could be denied.

Bibliography

[1] Yann LeCun, Yoshua Bengio, and Geoffrey Hinton. ‘Deep learning’. In: *nature* 521.7553 (2015), p. 436 (cited on pages 1, 5).

[2] Yann LeCun et al. ‘Handwritten Digit Recognition with a Back-Propagation Network’. In: *Advances in Neural Information Processing Systems*. Ed. by D. Touretzky. Vol. 2. Morgan-Kaufmann, 1989 (cited on pages 1, 20).

[3] R. Hadsell, S. Chopra, and Y. LeCun. ‘Dimensionality Reduction by Learning an Invariant Mapping’. In: *2006 IEEE Computer Society Conference on Computer Vision and Pattern Recognition (CVPR’06)*. Vol. 2. 2006, pp. 1735–1742. DOI: 10.1109/CVPR.2006.100 (cited on pages 3, 41).

[4] Ting Chen et al. ‘A Simple Framework for Contrastive Learning of Visual Representations’. In: *Proceedings of the 37th International Conference on Machine Learning, ICML 2020, 13-18 July 2020, Virtual Event*. Vol. 119. Proceedings of Machine Learning Research. PMLR, 2020, pp. 1597–1607 (cited on pages 3, 41, 42, 57, 58).

[5] Prannay Khosla et al. ‘Supervised Contrastive Learning’. In: *Advances in Neural Information Processing Systems*. Ed. by H. Larochelle et al. Vol. 33. Curran Associates, Inc., 2020, pp. 18661–18673 (cited on pages 3, 41, 57).

[6] Olivier Henaff. ‘Data-Efficient Image Recognition with Contrastive Predictive Coding’. In: *Proceedings of the 37th International Conference on Machine Learning*. Ed. by Hal Daumé III and Aarti Singh. Vol. 119. Proceedings of Machine Learning Research. PMLR, 13–18 Jul 2020, pp. 4182–4192 (cited on pages 3, 41).

[7] R. Devon Hjelm et al. ‘Learning deep representations by mutual information estimation and maximization’. In: *7th International Conference on Learning Representations, ICLR 2019, New Orleans, LA, USA, May 6-9, 2019*. 2019 (cited on pages 3, 41).

[8] Zhirong Wu et al. ‘Unsupervised Feature Learning via Non-parametric Instance Discrimination’. In: *2018 IEEE/CVF Conference on Computer Vision and Pattern Recognition*. Salt Lake City, UT: IEEE, June 2018, pp. 3733–3742. DOI: 10.1109/CVPR.2018.00393. (Visited on 06/20/2024) (cited on pages 3, 41).

[9] Carlo Alberto Barbano et al. ‘Anatomical Foundation Models for Brain MRIs’. In: *Submitted to Neural Information Processing Systems (NeurIPS)* (2024) (cited on page 4).

[10] Mathieu Blondel and Vincent Roulet. *The Elements of Differentiable Programming*. 2024 (cited on page 5).

[11] Simone Scardapane. *Alice’s Adventures in a Differentiable Wonderland – Volume I, A Tour of the Land*. 2024 (cited on page 5).

[12] Ian J. Goodfellow, Yoshua Bengio, and Aaron Courville. *Deep Learning*. http://www.deeplearningbook.org. Cambridge, MA, USA: MIT Press, 2016 (cited on page 5).

[13] Andreas Griewank and Andrea Walther. *Evaluating Derivatives*. Second. Society for Industrial and Applied Mathematics, 2008 (cited on page 9).

[14] R. E. Wengert. 'A simple automatic derivative evaluation program'. In: *Commun. ACM* 7.8 (1964), pp. 463–464. DOI: 10.1145/355586.364791 (cited on page 10).

[15] Adam Paszke et al. 'Automatic differentiation in PyTorch'. In: (2017) (cited on pages 14, 58).

[16] Martín Abadi et al. 'Tensorflow: A System for Large-Scale Machine Learning'. In: *12th Symposium on Operating Systems Design and Implementation*. 2016, pp. 265–283 (cited on page 14).

[17] Frank Rosenblatt. 'The Perceptron: A Probabilistic Model for Information Storage and Organization in the Brain'. In: *Psychological Review* 65 (1958), pp. 386–408 (cited on page 16).

[18] Frank Rosenblatt. *Principles of Neurodynamics*. Spartan Books, 1959 (cited on page 19).

[19] Moshe Leshno et al. 'Multilayer feedforward networks with a nonpolynomial activation function can approximate any function'. In: *Neural Networks* 6.6 (1993), pp. 861–867. DOI: https://doi.org/10.1016/S0893-6080(05)80131-5 (cited on page 19).

[20] Kunihiko Fukushima. 'Neocognitron: A self-organizing neural network model for a mechanism of pattern recognition unaffected by shift in position'. en. In: *Biological Cybernetics* 36.4 (Apr. 1980), pp. 193–202. DOI: 10.1007/BF00344251. (Visited on 06/15/2024) (cited on page 20).

[21] Alex Krizhevsky, Ilya Sutskever, and Geoffrey E Hinton. 'ImageNet Classification with Deep Convolutional Neural Networks'. In: *Advances in Neural Information Processing Systems*. Ed. by F. Pereira et al. Vol. 25. Curran Associates, Inc., 2012 (cited on page 24).

[22] Karen Simonyan and Andrew Zisserman. *Very Deep Convolutional Networks for Large-Scale Image Recognition*. 2015 (cited on page 24).

[23] Kaiming He et al. 'Deep Residual Learning for Image Recognition'. In: *Proceedings of 2016 IEEE Conference on Computer Vision and Pattern Recognition*. CVPR '16. IEEE, June 2016, pp. 770–778. DOI: 10.1109/CVPR.2016.90 (cited on pages 24, 25).

[24] Gao Huang et al. *Densely Connected Convolutional Networks*. 2018 (cited on page 24).

[25] Rahul S Desikan et al. 'An automated labeling system for subdividing the human cerebral cortex on MRI scans into gyral based regions of interest'. In: *Neuroimage* 31.3 (2006), pp. 968–980 (cited on pages 27, 36, 47, 54).

[26] V. P. Grover et al. 'Magnetic Resonance Imaging: Principles and Techniques: Lessons for Clinicians'. In: *J Clin Exp Hepatol* 5.3 (Sept. 2015), pp. 246–255 (cited on page 29).

[27] John Ashburner and Karl J. Friston. 'Voxel-Based Morphometry—The Methods'. In: *NeuroImage* 11.6 (2000), pp. 805–821. DOI: https://doi.org/10.1006/nimg.2000.0582 (cited on page 31).

[28] A.C. Evans et al. '3D statistical neuroanatomical models from 305 MRI volumes'. In: *1993 IEEE Conference Record Nuclear Science Symposium and Medical Imaging Conference*. 1993, 1813–1817 vol.3. DOI: 10.1109/NSSMIC.1993.373602 (cited on page 31).

[29] F. Kurth, E. Luders, and C. Gaser. 'Voxel-Based Morphometry'. In: *Brain Mapping*. Ed. by Arthur W. Toga. Waltham: Academic Press, 2015, pp. 345–349. DOI: https://doi.org/10.1016/B978-0-12-397025-1.00304-3 (cited on page 32).

[30] J. Ashburner and K. J. Friston. 'Unified segmentation'. In: *Neuroimage* 26.3 (July 2005), pp. 839–851 (cited on page 33).

[31] Antoine Grigis, Dorval Loïc, and Dollé Bérangère. *BrainPrep*. Version 0.0.1. 2022 (cited on pages 34, 56).

[32] Christian Gaser et al. 'CAT–A computational anatomy toolbox for the analysis of structural MRI data'. In: *biorxiv* (2022), pp. 2022–06 (cited on pages 34, 56).

[33] Bruce Fischl. 'FreeSurfer'. In: *NeuroImage* 62.2 (2012). 20 YEARS OF fMRI, pp. 774–781. DOI: https://doi.org/10.1016/j.neuroimage.2012.01.021 (cited on pages 34, 37).

[34] Simon B. Eickhoff, B. T. Thomas Yeo, and Sarah Genon. 'Imaging-based parcellations of the human brain'. en. In: *Nature Reviews Neuroscience* 19.11 (Nov. 2018), pp. 672–686. DOI: 10.1038/s41583-018-0071-7. (Visited on 06/28/2024) (cited on page 35).

[35] Pantea Moghimi et al. *A Review on MR Based Human Brain Parcellation Methods*. 2021. URL: https://arxiv.org/abs/2107.03475 (cited on page 35).

[36] C. Destrieux et al. 'Automatic parcellation of human cortical gyri and sulci using standard anatomical nomenclature'. In: *Neuroimage* 53.1 (Oct. 2010), pp. 1–15 (cited on page 36).

[37] H.M. Duvernoy et al. *The Human Brain: Surface, Three-Dimensional Sectional Anatomy with MRI, and Blood Supply*. Springer Vienna, 1999 (cited on page 38).

[38] Lan Lan et al. 'Generative Adversarial Networks and Its Applications in Biomedical Informatics'. In: *Frontiers in Public Health* 8 (May 2020), p. 164. DOI: 10.3389/fpubh.2020.00164. (Visited on 06/18/2024) (cited on page 39).

[39] Jia Deng et al. 'ImageNet: A large-scale hierarchical image database'. In: *2009 IEEE Conference on Computer Vision and Pattern Recognition*. 2009, pp. 248–255. DOI: 10.1109/CVPR.2009.5206848 (cited on page 39).

[40] Benoit Dufumier et al. 'Exploring the potential of representation and transfer learning for anatomical neuroimaging: Application to psychiatry'. In: *NeuroImage* 296 (2024), p. 120665. DOI: https://doi.org/10.1016/j.neuroimage.2024.120665 (cited on page 39).

[41] Florian Schroff, Dmitry Kalenichenko, and James Philbin. 'FaceNet: A unified embedding for face recognition and clustering.' In: *CVPR*. IEEE Computer Society, 2015, pp. 815–823 (cited on page 41).

[42] Kihyuk Sohn. 'Improved Deep Metric Learning with Multi-class N-pair Loss Objective'. In: *Advances in Neural Information Processing Systems*. Ed. by D. Lee et al. Vol. 29. Curran Associates, Inc., 2016 (cited on page 41).

[43] Aäron van den Oord, Yazhe Li, and Oriol Vinyals. 'Representation Learning with Contrastive Predictive Coding'. In: *CoRR* abs/1807.03748 (2018) (cited on page 43).

[44] Benoit Dufumier et al. 'Contrastive learning with continuous proxy meta-data for 3D MRI classification'. In: *Medical Image Computing and Computer Assisted Intervention–MICCAI 2021: 24th International Conference, Strasbourg, France, September 27–October 1, 2021, Proceedings, Part II 24*. Springer. 2021, pp. 58–68 (cited on page 44).

[45] Carlo Alberto Barbano et al. 'Contrastive learning for regression in multi-site brain age prediction'. In: *2023 IEEE 20th International Symposium on Biomedical Imaging (ISBI)*. IEEE. 2023, pp. 1–4 (cited on page 45).

[46] Benoit Dufumier et al. 'OpenBHB: a Large-Scale Multi-Site Brain MRI Data-set for Age Prediction and Debiasing'. In: *NeuroImage* 263 (Nov. 2022), p. 119637. DOI: 10.1016/j.neuroimage.2022.119637. (Visited on 02/19/2024) (cited on pages 47, 53, 54, 56).

[47] Vera Komeyer et al. 'A framework for confounder considerations in AI-driven precision medicine'. In: *medRxiv* (2024). Publisher: Cold Spring Harbor Laboratory Press. DOI: 10.1101/2024.02.02.24302198 (cited on page 47).

[48] Ronald Carl Petersen et al. 'Alzheimer's disease Neuroimaging Initiative (ADNI) clinical characterization'. In: *Neurology* 74.3 (2010), pp. 201–209 (cited on page 53).

[49] Pamela J LaMontagne et al. 'OASIS-3: longitudinal neuroimaging, clinical, and cognitive dataset for normal aging and Alzheimer disease'. In: *MedRxiv* (2019), pp. 2019–12 (cited on page 53).

[50] Lei Wang et al. 'SchizConnect: Mediating neuroimaging databases on schizophrenia and related disorders for large-scale integration'. In: *Neuroimage* 124 (2016), pp. 1155–1167 (cited on page 53).

[51] Adriana Di Martino et al. *ABIDE — fcon_1000.projects.nitrc.org*. https://fcon_1000.projects.nitrc.org/indi/abide/abide_I.html (cited on page 53).

[52] Irene Cumplido-Mayoral et al. 'Biological brain age prediction using machine learning on structural neuroimaging data: Multi-cohort validation against biomarkers of Alzheimer's disease and neurodegeneration stratified by sex'. In: *eLife* 12 (Apr. 2023). DOI: 10.7554/eLife.81067 (cited on page 59).

[53] Ann-Marie G De Lange and James H Cole. 'Commentary: Correction procedures in brain-age prediction'. In: (2020). DOI: 10.1016/j.nicl.2020.102229 (cited on page 59).

[54] Alec Radford et al. 'Learning Transferable Visual Models From Natural Language Supervision'. In: *Proceedings of the 38th International Conference on Machine Learning*. Ed. by Marina Meila and Tong Zhang. Vol. 139. Proceedings of Machine Learning Research. PMLR, 18–24 Jul 2021, pp. 8748–8763 (cited on page 66).

[55] Zifeng Wang et al. ‘MedCLIP: Contrastive Learning from Unpaired Medical Images and Text’. en. In: *Proceedings of the 2022 Conference on Empirical Methods in Natural Language Processing*. Abu Dhabi, United Arab Emirates: Association for Computational Linguistics, 2022, pp. 3876–3887. DOI: 10.18653/v1/2022.emnlp-main.256. (Visited on 06/18/2024) (cited on page 66).

[56] Janani Venugopalan et al. ‘Multimodal deep learning models for early detection of Alzheimer’s disease stage’. en. In: *Sci. Rep.* 11.1 (Feb. 2021), p. 3254 (cited on page 66).